

High-precision chemical abundances of Galactic building blocks. The distinct chemical abundance sequence of Sequoia

Tadafumi Matsuno¹, Helmer H. Koppelman², Amina Helmi¹, Wako Aoki³, Miho N. Ishigaki³, Takuma Suda⁴, Zhen Yuan⁵, and Kohei Hattori^{3,6}

¹ Kapteyn Astronomical Institute, University of Groningen, Landleven 12, 9747 AD Groningen, The Netherlands
e-mail: matsuno@astro.rug.nl

² School of Natural Sciences, Institute for Advanced Study, 1 Einstein Drive, Princeton, NJ 08540, USA

³ National Astronomical Observatory of Japan, 2-21-1 Osawa, Mitaka, Tokyo 181-8588, Japan

⁴ Department of Liberal Arts, Tokyo University of Technology, Ota-ku, Tokyo 144-8535, Japan

⁵ Université de Strasbourg, CNRS, Observatoire Astronomique de Strasbourg, UMR 7550, F-67000 Strasbourg, France

⁶ Institute of Statistical Mathematics, 10-3 Midoricho, Tachikawa, Tokyo 190-0014, Japan

July 7, 2023

ABSTRACT

Context. Sequoia is a retrograde kinematic substructure in the nearby Galactic halo, whose properties are a matter of debate. For example, previous studies do not necessarily agree on the chemical abundances of Sequoia stars, which are important for understanding its nature.

Aims. We characterize the chemical properties of a sample of stars from Sequoia by determining high-precision abundances.

Methods. We measured abundances of Na, Mg, Si, Ca, Ti, Cr, Mn, Ni, Zn, Y, and Ba from a differential abundance analysis on high signal-to-noise ratio, high-resolution spectra from new observations and from archival data. We compared precisely measured chemical abundances of 12 Sequoia candidates with those of typical halo stars from the literature, which also includes stars from Gaia-Enceladus. This allowed us to characterize Sequoia and compare it to another Galactic building block. The comparison was made after putting all the abundances onto the same scale using standard stars.

Results. There are significant differences in [Na/Fe], [Mg/Fe], [Ca/Fe], [Ti/Fe], [Zn/Fe], and [Y/Fe] between Sequoia and Gaia-Enceladus stars at $-1.8 \lesssim [\text{Fe}/\text{H}] \lesssim -1.4$ in the sense that these abundance ratios are lower in Sequoia. These differences are similar to those seen between Gaia-Enceladus and in situ stars at a higher metallicity, suggesting that Sequoia is affected by type Ia supernovae at a lower metallicity than Gaia-Enceladus. We also confirm that the low [Mg/Fe] of Sequoia is seen in the literature and in surveys, namely APOGEE DR17 and GALAH DR3, if the stars are kinematically selected in the same way.

Conclusions. Sequoia stars have a distinct chemical abundance pattern and can be chemically separated from in situ stars or Gaia-Enceladus stars if abundances are measured with sufficient precision, namely $\sigma([\text{X}/\text{Fe}]) \lesssim 0.07$ dex.

1. Introduction

The standard cosmological model predicts that galaxies grow through a hierarchical process. The Milky Way is no exception and has been shown to have accreted a number of dwarf galaxies. There is indeed evidence for the ongoing accretion in the form of stellar streams from the Sagittarius dwarf galaxy (e.g., Ibata et al. 1994; Belokurov et al. 2006; Grillmair 2006; Bernard et al. 2016; Malhan et al. 2018; Ramos et al. 2020; Antoja et al. 2020). However, in the case of ancient accretion events that deposited stars to the inner parts of the Galaxy, streams would have lost their spatial coherence. This is why chemodynamical analysis of halo stars is a powerful way to recover the accretion history of the Milky Way. Orbits and chemical abundances generally remain unchanged for a long time.

A number of studies have pointed out correlations between abundance ratios of halo stars and their kinematics (e.g., Nissen & Schuster 1997; Gratton et al. 2003; Venn et al. 2004; Nissen & Schuster 2010; Ishigaki et al. 2012). In particular, Nissen & Schuster (2010, hereafter NS10) clearly showed the presence of two chemically distinct stellar populations among nearby halo stars that also have different kinematics. They interpreted the population with a low $[\alpha/\text{Fe}]$ abundance ratio as a group of accreted stars from dwarf galaxies and the high- α population to

have formed in situ within the Milky Way. After the data releases from the Gaia mission (Gaia Collaboration et al. 2016, 2018), it became apparent that there is a kinematic overdensity of stars with radial orbits in the Galactic halo, known as the Gaia-Sausage (e.g., Belokurov et al. 2018; Koppelman et al. 2018). The kinematic overdensity turns out to follow the low- α population (e.g., Helmi et al. 2018; Haywood et al. 2018; Mackereth et al. 2019; Hasselquist et al. 2021) and it is now considered to be the debris from the last major merger that the Milky Way experienced and it has been named Gaia-Enceladus. The in situ halo stars with high [Mg/Fe] are likely those heated by this event from the disk present at that time (Helmi et al. 2018; Belokurov et al. 2020; Gallart et al. 2019; Di Matteo et al. 2019).

In addition to these two major populations, there seems to be an additional, highly retrograde component in the Milky Way halo. The Gaia data revealed that there is an overdensity of stars in the space of kinematics that has large retrograde motion and large orbital energy (e.g., Myeong et al. 2018; Koppelman et al. 2018; Yuan et al. 2020; Naidu et al. 2020), which is now widely called Sequoia. Since Sequoia is less prominent and has a lower mean metallicity than Gaia-Enceladus, this could be a disrupted dwarf galaxy smaller than Gaia-Enceladus (Myeong et al. 2019; Koppelman et al. 2019; Matsuno et al. 2019; Naidu et al. 2020; Feuillet et al. 2021). However, the picture is somewhat confus-

ing because the region occupied by Sequoia has been suggested to contain multiple components (Naidu et al. 2020). Helmi et al. (2018) suggest that the progenitor of Gaia-Enceladus can also deposit stars onto Sequoia-like orbits depending on the morphology and the inclination of its initial orbit, which is supported by numerical simulations (Koppelman et al. 2019). Another complication arises in the selection and definition of Sequoia stars; while Matsuno et al. (2019), Koppelman et al. (2019), Naidu et al. (2020), and Aguado et al. (2021) used selections in the angular momentum (L_z) and orbital energy (E) of the stars ($L_z - E$ selection), Myeong et al. (2019), Monty et al. (2020), and Feuillet et al. (2021) mostly used normalized actions (\mathcal{J} selection). In the latter case, the selected stars extend to a much lower orbital energy (e.g., Feuillet et al. 2021).

Chemical abundance analysis from high-resolution spectroscopy is crucial to understand the properties of Sequoia. Differences in abundance ratios imply different conditions of star formation, for example, star formation with a different efficiency, which, in turn, could be related to the mass of the progenitor galaxy and/or its environment. Although chemical abundance ratios have been well studied for Gaia-Enceladus, in situ stars, and surviving dwarf galaxies (e.g., Venn et al. 2004; Tolstoy et al. 2009; Nissen & Schuster 2010; Hasselquist et al. 2021), the current understanding about the chemical abundance ratios of Sequoia is much less clear.

Long before the discovery of Sequoia as a kinematic overdensity, Venn et al. (2004) pointed out the systematically low $[\alpha/\text{Fe}]$ ratios of highly retrograde stars; they showed that the very low $[\alpha/\text{Fe}]$ ratios seen among the outermost halo stars in Stephens & Boesgaard (2002) are rather related to their large retrograde motion. For the first time, Matsuno et al. (2019) have recently indicated the connection between Sequoia and the results from Venn et al. (2004). They selected stars in an overdensity with large retrograde motion at a high orbital energy ($L_z - E$ selection), which later named Sequoia, from the Stellar Abundances for Galactic Archaeology Database (Suda et al. 2008, 2011; Yamada et al. 2013; Suda et al. 2017). They show that the selected stars have, on average, lower $[\text{Na}/\text{Fe}]$, $[\text{Mg}/\text{Fe}]$, and $[\text{Ca}/\text{Fe}]$ than Gaia-Enceladus or in situ stars at $[\text{Fe}/\text{H}] \sim -1.5$. This conclusion is supported by Monty et al. (2020), who recalibrated the abundances and recalculated the kinematics of stars studied by Stephens & Boesgaard (2002). Among their Sequoia stars selected with the \mathcal{J} selection, stars with a low binding energy, corresponding to a $L_z - E$ selection, show low values of $[\text{Mg}/\text{Fe}]$ and $[\text{Ca}/\text{Fe}]$, while stars with a higher binding energy have higher Mg and Ca abundances. Additionally, the proper-motion pair, HD134439 and HD134440, which has large retrograde Galactic motion (King 1997; Lim et al. 2021) and indeed satisfies most of the $L_z - E$ selections, has been known to have low α -element abundances (King 1997; Chen & Zhao 2006; Chen et al. 2014; Reggiani & Meléndez 2018; Lim et al. 2021). Among these studies, Reggiani & Meléndez (2018) have indeed confirmed that the α -element abundances of HD134439 and HD134440 are even lower than NS10's low- α halo population. Data from GALAH DR3 also seem to support the low- α abundance of Sequoia (see α -element abundance presented in Aguado et al. 2021, who used a $L_z - E$ selection). The same feature is, however, not clearly seen in data from APOGEE as presented in Koppelman et al. (2019) with a $L_z - E$ selection, and Myeong et al. (2019) and Feuillet et al. (2021) with a \mathcal{J} selection.

In summary, several studies seem to have shown that Sequoia stars have lower α -element abundances than Gaia-Enceladus on average if they are selected according to L_z and E . However, the magnitude of the difference is comparable to the typical uncer-

tainties of abundance ratios for individual stars. This small difference together with the existence of multiple ways to kinematically select Sequoia stars have hampered a clear understanding. High-precision chemical abundance from a differential abundance analysis on high signal-to-noise (S/N) spectra would allow us to robustly detect the abundance difference, if any, as shown by Nissen & Schuster (2010, 2011) to be powerful to characterize the abundance difference between accreted and in situ halo stars.

The aim of this study is to carry out a high-precision abundance analysis for Sequoia stars selected by the $L_z - E$ selection using both newly obtained high-resolution spectra and archival spectra, and to compare the results with other halo stars. The comparison halo stars come from NS10 at $-1.5 \lesssim [\text{Fe}/\text{H}] \lesssim -0.7$ and Reggiani et al. (2017, R17), who carried out a high-precision abundance analysis for stars with $-2.5 \lesssim [\text{Fe}/\text{H}] \lesssim -1.5$. As we see below, we clearly detected very low- α element abundances for Sequoia stars. We describe our target selection and the data in Section 2 and the abundance analysis in Section 3. After briefly introducing our results in Section 4, we provide a discussion in Section 5 and present our conclusions in Section 6.

2. Observations and target selection

We obtained new high- S/N , high-resolution spectra for nine Sequoia member candidates with the Subaru Telescope (for eight stars) and with Magellan (for one star). Out of the nine stars, one star (Gaia EDR3 360456543361799808) turned out to have a very different radial velocity from the value used for the selection (see Appendix A), and hence it can no longer be regarded as a part of Sequoia. We also collected high- S/N archival high-resolution spectra for four Sequoia candidates and for three standard stars from Subaru, Keck, and Very Large Telescopes (VLT). The data and target information are summarized in Table 1 and Table 2, respectively.

The Subaru observations were conducted with the High Dispersion Spectrograph (HDS; Noguchi et al. 2002) from November 8–10, 2019. We used the standard setup StdYd of HDS, which provides a wavelength coverage of 4000–6800 Å, and the image slicer #2 (Tajitsu et al. 2012), which yields $R \sim 80,000$. Two to eight exposures were taken for each object and the total exposure time ranged from 20 minutes to 4 hours depending on the brightness of the stars. We reduced the data using an IRAF¹ script, `hdsq1`², which includes a CCD linearity correction, scattered light subtraction, aperture extraction, flat-fielding, wavelength calibration, and a heliocentric velocity correction.

The Magellan observation was conducted with the Magellan Inamori Kyocera Echelle (MIKE; Bernstein et al. 2003) on December 29, 2019. Although the MIKE spectrum has a wide spectral coverage from 3350 Å to 9300 Å, we only used 4000–6800 Å to maintain consistency with the HDS spectra. The slit width was 0.70'', which yields $R \sim 40,000$ for the region bluer than 4950 Å and $R \sim 32,000$ for the redder part.

We searched reduced archive spectra using the Japanese Virtual Observatory portal for archive HDS spectra³, the Keck Observatory Archive (KOA) for data taken with the High Resolu-

¹ IRAF is distributed by the National Optical Astronomy Observatory, which is operated by the Association of Universities for Research in Astronomy (AURA) under a cooperative agreement with the National Science Foundation

² <http://www.subarutelescope.org/Observing/Instruments/HDS/hdsq1-e.html>

³ <http://jvo.nao.ac.jp/portal/subaru/hds.do>

Table 1. Summary of the data

Object	Gaia EDR3 source id	Telescope	Resolution	S/N_1	S/N_2	S/N_3
1336_6432	1336408284224866432	Subaru	80,000	94	139	137
2657_5888	2657496656325125888	Subaru	80,000	41	79	92
2813_6032	2813331813720876032	Subaru	80,000	130	173	126
2870_9072	2870313110476579072	Subaru	80,000	88	118	52
3336_0672	3336204190352220672	Subaru	80,000	90	194	114
3341_2720	3341934256545182720	Subaru	80,000	126	140	99
4587_5616	4587905579084735616	Subaru	80,000	48	81	75
4850_5696	4850673911632285696	Magellan	32,000–40,000	207	128	176
G90-36	876358870971624320	Keck	48,000	41	67	50
G115-58	1011379899590855936	Subaru	100,000	90	147	98
HIP28104	2910503176753011840	VLT	50,000	93	161	181
HIP98492	4299974407538484096	Keck	72,000	77	133	83
G112-43	3085891537839267328	Subaru	100,000	214	208	99
CD–48°02445	5551565291043498496	VLT	50,000	130	289	258
HD59392	5586241315104190848	VLT	50,000	170	441	248

Notes. We obtained new high-resolution spectra for the eight Sequoia stars in the first group, and archival high-resolution spectra for the four Sequoia stars in the second group and for the three standard stars in the last group. The S/N_1 , S/N_2 , and S/N_3 were measured at around 4500, 5533, and 6370 Å, respectively, and converted to per 0.01 Å.

tion Echelle Spectrometer (HIRES; Vogt et al. 1994) on Keck, and European Southern Observatory Science Archive Facility for data taken with the Ultraviolet and Visual Echelle Spectrograph (UVES; Dekker et al. 2000). In the present study, we used archive spectra for four Sequoia stars and three standard stars (Table 1).

All the spectra were normalized by fitting continua with cubic splines after combining multiple exposures for individual objects. For objects for which we conducted new observations, the radial velocity was measured by comparing the observed wavelengths of Fe I absorption lines with the values measured by laboratory experiments. We adopted literature measurements of radial velocities for stars for which spectra were taken from archives (Table 2).

All the candidate Sequoia member stars were selected based on their angular momentum around the z -axis of the Milky Way (L_z) and orbital energy (E). We combined Gaia DR2 astrometry with radial velocity measurements provided in Gaia DR2 and LAMOST DR4 for the target selection. Table 2 and Figure 1 include updated kinematic information for the program stars, where astrometry is now taken from Gaia EDR3 and the radial velocity comes from high-resolution spectroscopy. Although we updated the astrometry and radial velocity, the orbital parameters obtained did not change significantly. Here we assumed that the Sun is located at $R_0 = 8.21$ kpc (McMillan 2017) and $z_0 = 20.8$ pc (Bennett & Bovy 2019) and moving at 11.1 km s $^{-1}$ toward the Galactic anticenter (Schönrich et al. 2010), 245.3 km s $^{-1}$ in the Galactic rotation direction (Reid & Brunthaler 2004; McMillan 2017), and 7.25 km s $^{-1}$ toward the Galactic north pole (Schönrich et al. 2010). The Milky Way potential used is from McMillan (2017). The calculation of the orbital energy was conducted with the software AGAMA (Vasiliev 2019). We estimated uncertainties through a Monte Carlo method. All the Sequoia candidates have $L_z < -1600$ kpc km s $^{-1}$ and $E > -1.3 \times 10^5$ km 2 s $^{-2}$. We also removed stars with $[\text{Fe}/\text{H}] > -1.0$ if they had metallicity estimates from LAMOST.

We note that our kinematic selections are based on our knowledge from Gaia DR2. In addition, updated selections will

be available with more recent and future Gaia data releases (see Lövdal et al. 2022; Ruiz-Lara et al. 2022).

To suppress the effect of systematic uncertainties that depend on stellar spectral types and to put our derived abundances onto the same scale as previous studies, we limited the sample to stars around the main-sequence turn-off region using the Gaia DR2 color-magnitude diagram. The updated photometric information with Gaia EDR3 is summarized in Table 2 and Figure 1. The extinction was estimated using the three-dimensional dust map by Green et al. (2019) and the extinction coefficients were estimated following Casagrande et al. (2021). For three objects, 4850_5696, HD59392, and CD–48°02445 not in the coverage of Green et al. (2019), we assumed their extinctions to be negligible since Ruiz-Dern et al. (2018) and Lallement et al. (2019) provide very small estimates for them ($E(B-V) < 0.01$). We note that two stars (2657_5888 and 4587_5616) lie along metal-rich isochrones. We discuss possible origins of the offset and effects on derived abundances in Appendix B.

We note that two additional stars (BD+09 2190 and HE1509-0252) were included in the list of Sequoia candidates with archive spectra, but they are not analyzed in the present study. These two objects have a much lower metallicity ($[\text{Fe}/\text{H}] = -2.63$ (Ishigaki et al. 2012) and -2.85 (Cohen et al. 2013), respectively) than the rest of the sample, and hence they are not suitable for the differential abundance analysis conducted in this study. The removal of these two stars and the metallicity selection ($[\text{Fe}/\text{H}] < -1.0$) for LAMOST stars result in narrower metallicity dispersion among our sample (0.19 dex) compared to ~ 0.3 dex reported for Sequoia in the literature (e.g., Matsuno et al. 2019).

To compare the properties of Sequoia stars with those of in situ and Gaia-Enceladus stars, we contrast chemical abundances of our Sequoia candidates with stars studied by NS10 and R17. These stars are also plotted in Figure 1 and cover a similar region of the color magnitude diagram. The orbital parameters of most of the NS10 stars and R17 stars are clearly different from the region of Sequoia. We note that the most retrograde star in the R17 sample is HIP28104, which is regarded as a Sequoia member candidate and is included in our analysis. The abundance of

Table 2. Target information

Object	π (mas)	$\sigma(\pi)$ (mas)	G	$B_p - R_p$	$E(B - V)$	RV (km s ⁻¹)	L_z (kpc km s ⁻¹)	$\sigma(L_z)$ (kpc km s ⁻¹)	E ($\times 10^5$ km ² s ⁻²)	$\sigma(E)$ ($\times 10^5$ km ² s ⁻²)
1336_6432	2.770	0.011	11.735	0.626	0.038	-560.2	-3000	12	-1.022	0.005
2657_5888	1.798	0.024	13.960	0.924	0.024	-348.4	-2934	52	-0.936	0.031
2813_6032	2.929	0.020	11.922	0.707	0.098	-461.9	-1787	12	-1.218	0.005
2870_9072	1.397	0.017	12.885	0.855	0.116	-392.1	-1628	25	-1.258	0.019
3336_0672	5.875	0.030	11.603	0.794	0.000	-13.9	-1722	26	-1.251	0.011
3341_2720	1.344	0.014	13.281	0.792	0.130	-137.3	-2478	92	-0.893	0.038
4587_5616	3.675	0.019	12.771	0.929	0.010	-600.2	-3147	9	-1.016	0.004
4850_5696	3.981	0.014	10.987	0.616	0.0	430.4	-1604	11	-1.299	0.003
G90-36	4.120	0.013	12.559	0.828	0.004	267.4	-2880	46	-1.004	0.019
G115-58	2.224	0.019	11.973	0.657	0.036	226.2	-1799	62	-1.246	0.017
HIP28104	2.590	0.011	12.080	0.620	0.014	253.6	-2504	30	-1.110	0.019
HIP98492	2.660	0.018	11.373	0.898	0.076	-266.4	-1791	36	-1.229	0.028
G112-43	5.595	0.019	10.063	0.686	0.000					
CD-48°02445	5.369	0.014	10.418	0.616	0.0					
HD59392	6.382	0.013	9.576	0.685	0.0					

Notes. Parallax and photometric information from Gaia EDR3. The extinction coefficient is from Green et al. (2019), except for 4850_5696, CD-48°02445, and HD59392, for which $E(B - V) = 0.0$ is assumed. Radial velocity is from our newly obtained spectra, except for G90-36, HIP28104 (Stephens & Boesgaard 2002), G115-58 (Ishigaki et al. 2012), and HIP98492 (O'Malley et al. 2017).

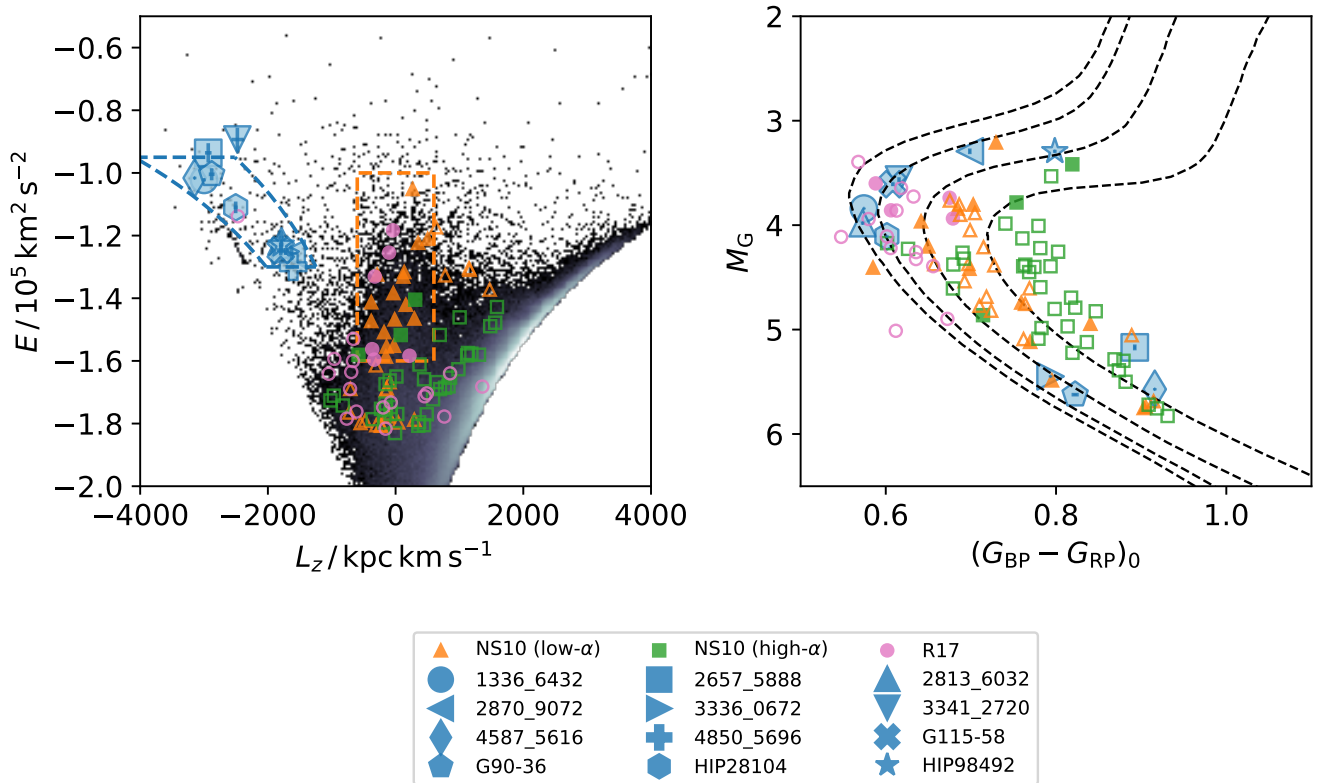


Fig. 1. Kinematic and photometric properties of the stars. Left: Angular momentum and orbital energy of the observed stars and the comparison stars. We also show the distribution of all stars in Gaia EDR3 with good astrometry (a relative parallax uncertainty smaller than 20%) and Gaia DR2 radial velocity. The blue dotted lines represent the Sequoia selection from Koppelman et al. (2019). Stars in the orange box are used to define the chemical abundance trends of Gaia-Enceladus. NS10 and R17 stars within this box are shown with filled symbols, while those outside of it are shown with open symbols. Right: Gaia EDR3 color-magnitude diagram of the program stars. We also plotted four PARSEC isochrones with the age of 12 Gyr and $[\text{Fe}/\text{H}] = -2.0, -1.5, -1.0,$ and -0.5 (from left right). We note that only stars with available extinction estimates from Green et al. (2019) are plotted for the NS10 and R17 samples.

this star reported by R17 is marked in all our abundance figures with a special symbol.

3. Abundance analysis

We derived stellar parameters and chemical abundances based on a differential abundance analysis adopting HD59392 as the reference star. Together with the high quality of the data, this approach enabled us to achieve high precision abundance measurements. In this section, we describe the analysis method, validate the results by comparing them with the literature, and homogenize abundances from the present study, NS10, and R17. For the abundance analysis, we used the November 2019 version of MOOG (Snedden 1973) through a python wrapper, q^2 (Ramírez et al. 2014), and adopted the standard MARCS model atmospheres (Gustafsson et al. 2008).

3.1. Equivalent widths measurements

Table 3 provides the line list and measured equivalent widths (EW). The line selection follows NS10 and R17, but the $\log gf$ values were updated for homogenization purposes. We measured equivalent widths of the lines by fitting Voigt profiles, of which the results were visually inspected. Stellar parameter determination and subsequent elemental abundance measurements

are based on these measured equivalent widths unless otherwise stated. Spectral synthesis was applied to Si, Mn, Zn, and Y. The equivalent widths of the lines from these elements were not measured by the Voigt profile fitting, but they are estimates based on a synthetic spectrum. Hyperfine structure splitting was taken into consideration for Na, Mn, and Ba.

We have two and three stars in common with NS10 and R17, respectively. The equivalent widths measured from archive spectra are compared with the values reported in the literature for these objects in Figures 2 and 3⁴. In comparison with NS10, G112-43 particularly offers an opportunity to confirm that different telescopes yield consistent spectra because we used a Subaru/HDS archive spectrum for this object (Table 1), while NS10 used one from VLT/UVES. We find excellent agreement in the comparison with NS10 for HD59392 and for G112-43. The average differences in reduced equivalent widths ($REW = \log(EW/\lambda)$) are $\Delta REW = -0.004$ ($\sigma = 0.029$) and $\Delta REW = 0.007$ ($\sigma = 0.041$), respectively.

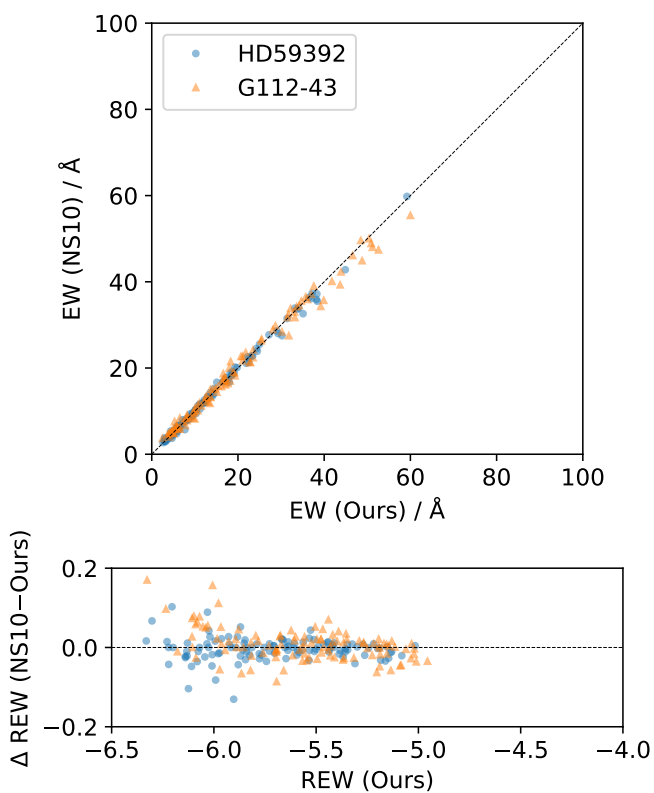
The agreements with R17 are also good, but our measured equivalent widths are larger than theirs for large equivalent widths, which is likely due to the different assumption for the line shape (Voigt and Gaussian profiles). We confirmed that Voigt profiles provide better fits for the strongest lines than Gaus-

⁴ The equivalent widths for the objects in R17 were kindly provided by H. Reggiani in private communication.

Table 3. Linelist and line-by-line abundance

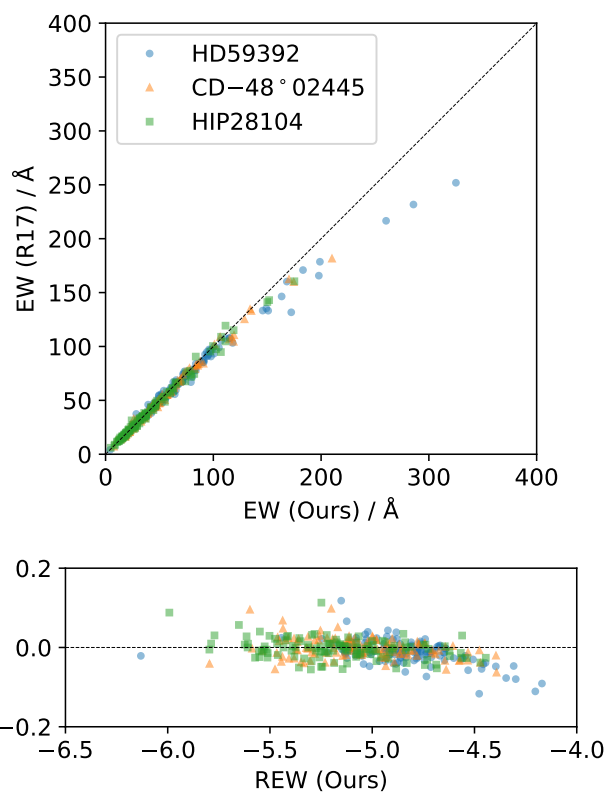
Object	species	λ (Å)	χ (eV)	$\log gf$	EW (mÅ)	$\sigma(EW)$ (mÅ)	$A(X)$ (dex)
1336_6432	NaI	5889.959	0.000	-0.193	133.6	6.2	4.230
1336_6432	NaI	5895.910	0.000	-0.575	107.0	5.0	4.108
1336_6432	MgI	4167.271	4.346	-0.746	43.7	2.1	5.969
1336_6432	MgI	5167.321	2.709	-0.854	125.8	5.8	6.125
1336_6432	MgI	5172.684	2.712	-0.363	173.0	8.0	6.118
$\sigma(A)_{T_{\text{eff}}}$ (dex)	$\sigma(A)_{\log g}$ (dex)	$\sigma(A)_{v_t}$ (dex)	$\sigma(A)_{[\text{Fe}/\text{H}]}$ (dex)	$\sigma(A)_{EW}$ (dex)	s_X (dex)	weight	
0.053	-0.009	-0.030	-0.003	0.108	0.000	60.883	
0.034	-0.003	-0.024	0.007	0.099	0.000	78.054	
0.026	-0.003	-0.003	0.001	0.053	0.000	204.968	
0.055	-0.012	-0.023	0.001	0.096	0.000	21.625	
0.064	-0.017	-0.014	0.001	0.080	0.000	10.299	

Notes. The full table is available online at CDS and a portion of the table is shown here.


Fig. 2. Equivalent width comparison with NS10.

sian profiles through visual inspection. Despite the offset at large equivalent widths, the average differences in reduced equivalent widths are small for all three objects ($\Delta REW = -0.012$, $\sigma = 0.030$ for HD59392; $\Delta REW = -0.001$, $\sigma = 0.026$ for CD-48°02445; and $\Delta REW = -0.001$, $\sigma = 0.029$ for HIP28104).

We estimated the uncertainties in the equivalent widths using the formula provided by Cayrel (1988). Although the formula predicts very small fractional uncertainties for strong lines, Figures 2 and 3 both show that this is not the case. Since this holds true even for the strongest lines, this is not likely dependent on S/N . Therefore, based on the scatter in ΔREW at


Fig. 3. Equivalent width comparison with R17. We note that this figure has a wider range in equivalent widths compared to Figure 2.

$-5.5 < REW < -4.5$, which is $0.015 - 0.025$ dex, we quadratically added 0.02 dex, which is equivalent to 4.6%, as an error floor to the uncertainties on the equivalent widths.

3.2. Stellar parameter determination

We determined the stellar parameters by combining an analysis of iron lines, as well as photometric and astrometric information from the Gaia mission. We estimated the effective temperature (T_{eff}) and microturbulent velocity (v_t) by minimizing the correlation coefficients between iron abundances derived from

individual neutral iron lines, and excitation potentials and REW , respectively.

We calculated the surface gravity ($\log g$) from

$$\begin{aligned}\log g &= \log g_{\odot} + \log(M/M_{\odot}) - 2 \log(R/R_{\odot}) \\ &= \log g_{\odot} + \log(M/M_{\odot}) + 4 \log(T_{\text{eff}}/T_{\text{eff},\odot}) - \log(L/L_{\odot})\end{aligned}$$

where M , R , and L are the mass, radius, and luminosity of the star, respectively. The mass was obtained by finding the stellar model that describes the position of the star in the color-absolute magnitude diagram best. Three parameters, age (τ), initial mass (M_{ini}), and $[\text{Fe}/\text{H}]_{\text{model}}$, were varied to find the best model. We maximized $p(\theta|\mathbf{x})$ through an ensemble Markov chain Monte Carlo sampling using emcee (Foreman-Mackey et al. 2013), where θ is $(\tau, M_{\text{ini}}, [\text{Fe}/\text{H}]_{\text{model}})$, \mathbf{x} is $(M_G, (Bp - Rp)_0, [\text{Fe}/\text{H}]_{\text{input}})$, and $p(\theta|\mathbf{x}) \propto L(\mathbf{x}|\theta)p(\theta)$. The likelihood $L(\mathbf{x}|\theta)$ was expressed as a multivariate Gaussian distribution $\mathcal{N}(\mathbf{x}_{\text{model}}|\mathbf{x}_{\text{obs}}, \Sigma)$, in which Σ reflects the observational uncertainties. For the uncertainty of M_G and $(Bp - Rp)_0$ and the covariance between the two, we considered the uncertainty in Gaia photometry and parallax, and extinction. We adopted a 0.2 dex uncertainty for $[\text{Fe}/\text{H}]_{\text{sp}}$ to take systematic uncertainties into account. We used the initial mass function of Kroupa & Weidner (2003) as the prior for the M_{ini} and a flat prior for the age between 1 and 20 Gyr. The luminosity was obtained from M_G and the bolometric correction by Casagrande & VandenBerg (2018).

First estimates of the uncertainties in the stellar parameters were obtained in the following way: the uncertainties in T_{eff} and v_t were estimated by finding the ranges of the values that provide the corresponding correlation coefficients consistent with zero at the 1σ level; the $\log g$ uncertainty was computed by randomly sampling M and L in Eq. 1 following their uncertainties, where covariances between M , T_{eff} , and L were assumed to be negligible; and the uncertainty of $[\text{Fe}/\text{H}]_{\text{sp}}$ was obtained from the standard deviation of the iron abundances from individual lines divided by the square root of the number of lines used. These estimates, however, do not take correlations between parameters into consideration. For example, since $[\text{Fe}/\text{H}]_{\text{sp}}$ clearly depends on the assumed values of the other parameters, we need to propagate the uncertainties in the other parameters into the uncertainty estimate for $[\text{Fe}/\text{H}]_{\text{sp}}$. We corrected the estimated uncertainties by properly considering the correlations between parameters following the method described in Appendix C. As a result of this procedure, we also obtained covariances between the estimated parameters.

Since we adopted a differential abundance analysis, the parameters of the standard star HD59392 determine the scale of our parameters. We adopted $T_{\text{eff}} = 6012$ K and $[\text{Fe}/\text{H}]_{\text{sp}} = -1.6$ (NS10), and we re-determined $\log g$ using the astrometric information. The microturbulence was updated to $v_t = 1.4$ km s $^{-1}$ so that the neutral iron abundances derived from individual lines do not depend on the line strength.

The stellar parameters and their uncertainties obtained as just described are provided in Table 4. We note that the $[\text{Fe}/\text{H}]_{\text{sp}}$ values in Table 4 are not the same as $[\text{Fe}/\text{H}]_{\text{I}}$ or $[\text{Fe}/\text{H}]_{\text{II}}$ which we report in the next section. This is because the computation of weights we use in the next section for abundance and its uncertainty estimates requires predetermined stellar parameters and their uncertainties. Since the stellar parameter determination process itself needs an iterative process, here, we adopted the simple mean of the abundances from individual lines to simplify the computation while we consider a weighted average in the next section.

3.3. Elemental abundances

Elemental abundances were obtained through a differential abundance analysis, assuming a one-dimensional plane-parallel atmosphere and local thermodynamic equilibrium (1D/LTE), except for Na. Since a Na abundance was sometimes derived from the Na D lines, the deviation from LTE can be significant. We corrected for this effect using the grid provided by Lind et al. (2011), which is available through the INSPECT database⁵.

For each species, abundances from individual lines were combined to obtain the best estimate for the abundance of the species following the prescription by Ji et al. (2020). In short, the final abundance is a weighted mean of the abundances from individual lines. The weight for a line reflects the uncertainty in its equivalent width and the sensitivity of the abundance to stellar parameters. An error floor (s_X) was added for individual lines so that the log likelihood,

$$\log \mathcal{L} = -\frac{1}{2} \sum \frac{(A_i - \bar{A})^2}{\sigma^2(A_i)_{EW} + s_X^2} \quad (2)$$

$$-\frac{1}{2} \sum \log(\sigma^2(A_i)_{EW} + s_X^2) + \text{constants}, \quad (3)$$

where A_i and \bar{A} are the abundance derived from individual lines and the best estimate of the abundance, respectively, is maximized. The abundance ratios $[X/Y]$ were computed with the correlation between the two elemental abundances taken into account. When computing $[X/\text{Fe}]$, we used the iron abundance from the same ionization state as the species X. We indicate 1σ confidence error ellipses for Sequoia stars in the abundance figures to visualize the uncertainties and the covariance of the measured abundances. The information on abundances derived from individual lines, their sensitivities to the uncertainties in stellar parameters and equivalent widths, weights, and error floors are included in Table 3.

As stated earlier, the abundances from our analysis, and those from NS10, Nissen & Schuster (2011), and R17 were put into the same scale. Our abundances are anchored to NS10 using the abundance of HD59392. Although HD59392 was also analyzed by R17, it is located at the high metallicity end of their sample, and hence has large measurement uncertainties in their study. Therefore, we used CD-48°02445, which is one of the standard stars used by R17, to move the abundances of R17 into the same scale as ours. Specifically, we added offsets to the R17 abundances so that the abundance of CD-48°02445 from our analysis and that from their analysis are consistent. We note that the Na abundance of CD-48°02445 was incorrectly reported in R17 and the correct value is $[\text{Na}/\text{Fe}] = -0.309$ (H. Reggiani 2021 private communication). We adopted this correct value to shift the R17 abundances. We also note that the metal-poor half of the R17 sample was analyzed relative to HD338529 and not to CD-48°02445. Therefore, it is possible that R17 stars below $[\text{Fe}/\text{H}] \lesssim -2.1$ are not on the same abundance scale as the rest of the stars in R17 and stars in the present study and NS10.

The adopted abundances are summarized in Table D.1 for Sequoia stars and in Table 5 for the standard stars. We note that the abundance of HD59392 listed in Table 5 was exactly the same as the one provided in NS10.

Table 4. Stellar parameters

Object	T_{eff} (K)	$\sigma(T_{\text{eff}})$ (K)	$\log g$ (dex)	$\sigma(\log g)$ (dex)	v_i (km s ⁻¹)	$\sigma(v_i)$ (km s ⁻¹)	[Fe/H] _{sp} (dex)	σ ([Fe/H] _{sp}) (dex)	$\rho T_{\text{eff}, \log g}$	$\rho T_{\text{eff}, v_i}$	$\rho T_{\text{eff}, [\text{Fe}/\text{H}]_{\text{sp}}}$	$\rho_{\log g, v_i}$	$\rho_{\log g, [\text{Fe}/\text{H}]_{\text{sp}}}$	$\rho_{v_i, [\text{Fe}/\text{H}]_{\text{sp}}}$
1336_6432	6475	65	4.166	0.034	1.512	0.102	-1.691	0.030	0.485	0.269	0.280	0.108	0.448	-0.540
2657_5888	5317	152	4.314	0.056	0.784	0.530	-1.535	0.053	0.845	0.925	-0.751	0.749	-0.504	-0.807
2813_6032	6414	63	4.209	0.035	1.624	0.102	-1.662	0.029	0.425	0.435	0.206	0.071	0.468	-0.264
2870_9072	5815	60	3.788	0.046	1.272	0.066	-1.467	0.023	0.351	0.704	0.272	0.123	0.743	0.035
3336_0672	5575	148	4.471	0.051	1.062	0.427	-1.691	0.033	0.816	0.951	-0.542	0.738	-0.228	-0.625
3341_2720	6538	78	4.082	0.038	1.456	0.124	-1.831	0.031	0.537	0.355	0.355	0.169	0.525	-0.425
4587_5616	5481	80	4.496	0.033	1.329	0.235	-1.768	0.048	0.661	0.688	-0.304	0.343	0.009	-0.470
4850_5696	6448	65	4.194	0.033	1.415	0.107	-1.728	0.027	0.455	0.665	0.018	0.265	0.357	-0.287
G90-36	5394	46	4.476	0.030	1.210	0.172	-1.670	0.045	0.262	0.553	-0.306	-0.069	0.236	-0.491
G115-58	6187	69	4.012	0.041	1.361	0.069	-1.394	0.021	0.309	0.670	0.126	-0.023	0.770	-0.249
HIP28104	6468	45	4.247	0.042	1.339	0.090	-1.986	0.027	0.255	0.507	0.143	0.073	0.539	-0.126
HIP98492	5510	40	3.726	0.037	1.130	0.062	-1.272	0.021	0.199	0.526	-0.171	-0.170	0.713	-0.358
G112-43	6125	54	4.086	0.031	1.412	0.070	-1.286	0.019	0.421	0.695	0.137	0.117	0.626	-0.214
CD-48°02445	6446	58	4.205	0.036	1.457	0.111	-1.852	0.025	0.421	0.695	0.005	0.244	0.425	-0.310
HD59392	6012		3.954		1.400		-1.600							

Notes. The last three stars are standard stars and not part of Sequoia.

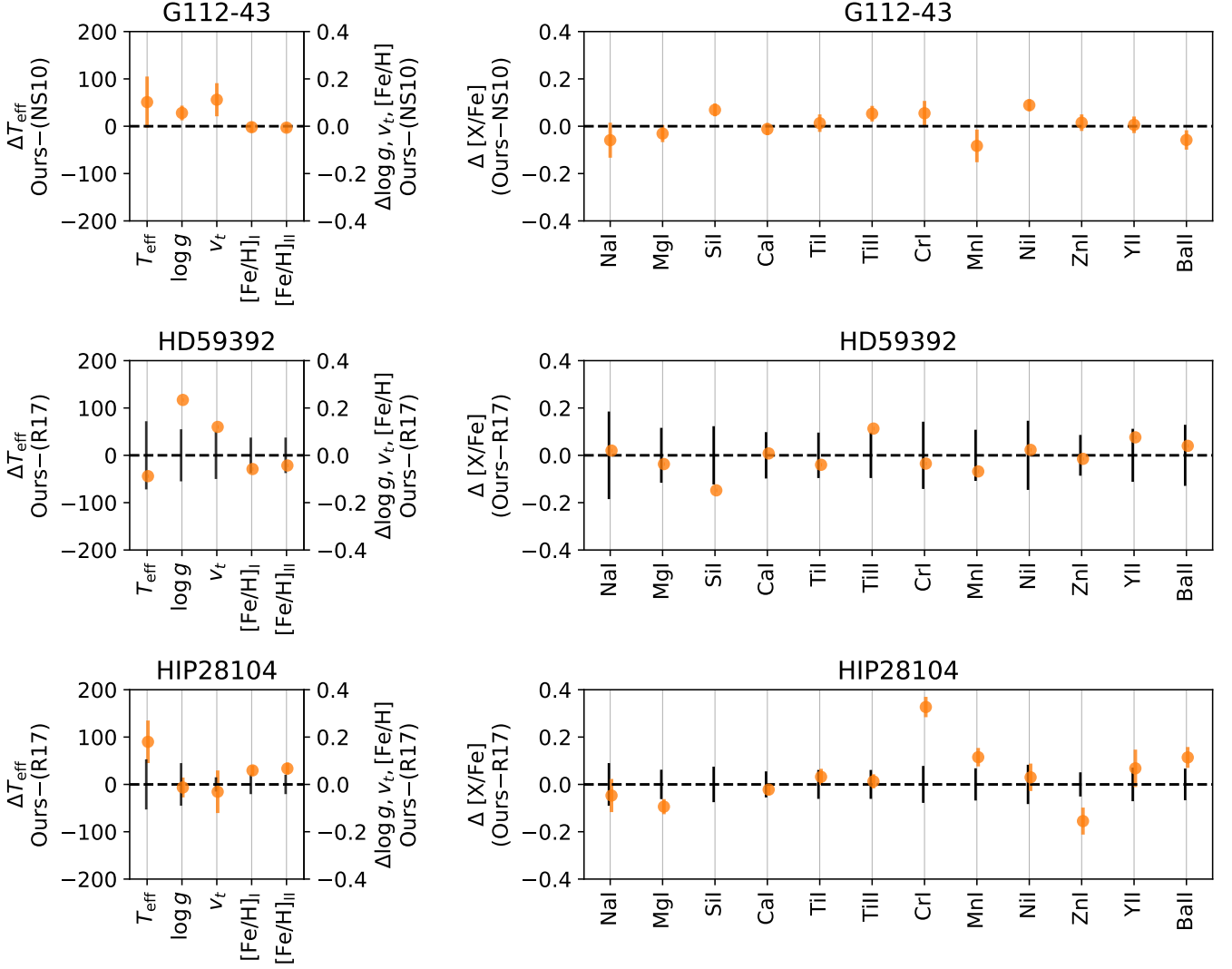


Fig. 4. Stellar parameter and abundance comparison with NS10 (G112-43) and R17 (HD59392 and HIP28104). The black error bars reflect the uncertainties reported in the literature.

3.4. Comparison with the literature

In this section, we compare the stellar parameters and chemical abundances of standard stars with the literature. For this purpose, we use G112-43 for the comparison with NS10 and HD59392 and HIP28104 for the comparison with R17. This comparison is presented in Figure 4.

There is excellent agreement in the abundance of G112-43 with NS10. The difference in $[X/Fe]$ is smaller than 0.1 dex in all of the elements. The differences are smaller than two times our measurement uncertainties for most of the species. We therefore consider that we successfully put our abundance onto NS10's scale using the standard star and that our uncertainty estimates are not underestimated. The exceptions are Si and Ni, for which our abundances differ from NS10's measurements by more than a 2σ uncertainty (2.3σ and 3.6σ , respectively). However, we note that we have not taken the measurement uncertainties in NS10 into account here since NS10 do not provide measurement uncertainties for individual objects.

⁵ Data obtained from the INSPECT database, version 1.0 (www.inspect-stars.net)

We now compare our results with R17. Since HD59392 is the standard star, there is no uncertainty in our abundance. The difference between the adopted abundance of HD59392 is consistent with R17 within the uncertainties reported by R17. Therefore, we have successfully put all the abundances onto the same scale for our study, NS10, and R17. We note that HIP28104 shows large difference in $[X/Fe]$, especially for Cr and Zn. Since HIP28104 was not analyzed relative to CD-48°02445 in R17 (see Section 3.3), the large offset is likely due to the use of different standard stars in R17.

4. Results

In this section, we compare the chemical abundance of stars in the present study with those in NS10 and R17. We kinematically selected Gaia-Enceladus stars out of NS10 and R17 samples using L_z and E_n as $|L_z| < 600 \text{ kpc km s}^{-1}$ and $-1.6 < E/10^5 \text{ km}^2 \text{ s}^{-2} < -1.0$ (Figure 1). We have 19 NS10 stars and six R17 stars that satisfy the Gaia-Enceladus kinematic selection. Among the 19 kinematically selected stars from NS10, 16 stars belong to their low- α population, confirming previous findings on the chemical abundance of Gaia-Enceladus. One of the

Table 5. Abundances of standard stars

G112-43					
	N	$[X/H]$	σ	$[X/Fe]$	σ
FeI	100	-1.254	0.022
FeII	10	-1.256	0.019
NaI	3	-1.423	0.076	-0.169	0.074
MgI	5	-1.075	0.038	0.179	0.036
SiI	5	-1.035	0.025	0.219	0.027
CaI	16	-0.977	0.028	0.278	0.025
TiI	11	-0.951	0.044	0.303	0.037
TiII	7	-0.914	0.035	0.343	0.033
CrI	6	-1.200	0.058	0.055	0.052
MnI	4	-1.527	0.071	-0.273	0.069
NiI	20	-1.185	0.029	0.069	0.025
ZnI	2	-0.940	0.036	0.315	0.035
YII	2	-1.390	0.037	-0.134	0.035
BaII	3	-1.584	0.044	-0.328	0.041
CD-48°02445					
	N	$[X/H]$	σ	$[X/Fe]$	σ
FeI	111	-1.814	0.025
FeII	11	-1.829	0.021
NaI	2	-2.091	0.082	-0.276	0.079
MgI	6	-1.563	0.035	0.251	0.033
SiI	2	-1.414	0.111	0.400	0.112
CaI	23	-1.461	0.026	0.353	0.025
TiI	10	-1.372	0.051	0.442	0.043
TiII	14	-1.540	0.032	0.289	0.031
CrI	5	-1.786	0.049	0.028	0.041
MnI	7	-2.161	0.048	-0.346	0.042
NiI	13	-1.844	0.044	-0.029	0.040
ZnI	1	-1.657	0.045	0.158	0.043
YII	2	-1.749	0.043	0.080	0.040
BaII	4	-1.985	0.044	-0.156	0.041
HD59392					
	N	$[X/H]$	σ	$[X/Fe]$	σ
FeI	134	(-1.600)	...	(...)	...
FeII	20	(-1.600)	...	(...)	...
NaI	4	(-1.750)	...	(-0.150)	...
MgI	7	(-1.320)	...	(0.280)	...
SiI	8	(-1.330)	...	(0.270)	...
CaI	23	(-1.220)	...	(0.380)	...
TiI	16	(-1.270)	...	(0.330)	...
TiII	14	(-1.270)	...	(0.330)	...
CrI	6	(-1.600)	...	(0.000)	...
MnI	8	(-1.960)	...	(-0.360)	...
NiI	26	(-1.610)	...	(-0.010)	...
ZnI	2	(-1.460)	...	(0.140)	...
YII	2	(-1.470)	...	(0.130)	...
BaII	4	(-1.670)	...	(-0.070)	...

Notes. The abundance of HD59392 is identical to NS10 since this is the reference star in our analysis.

remaining three stars is at $[Fe/H] = -1.08$ and clearly has a high- α abundance, which is clearly different from the rest of the Gaia-Enceladus stars. Thus, we removed this star from the Gaia-Enceladus sample. We kept the remaining two stars from NS10’s high- α population, since they are at $[Fe/H] \sim -1.4$, where the low- α and high- α populations begin to overlap. We thus ended up with 24 Gaia-Enceladus stars from the literature, which provide us with opportunities to compare abundance patterns of our Sequoia stars with those of Gaia-Enceladus stars.

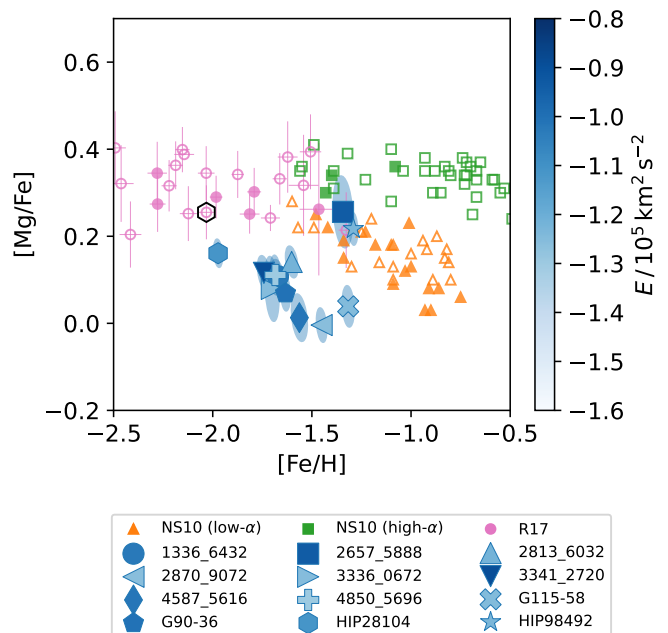


Fig. 5. Mg abundance of the stars. Kinematically selected Sequoia stars are plotted with blue symbols and color-coded according to their orbital energy (see Figure 1). The measurement uncertainty and the covariance between $[Mg/Fe]$ and $[Fe/H]$ are indicated by the error ellipses. The data point circled with a black hexagon from R17 indicates the abundance of HIP28104. The abundance of the comparison samples comes from Nissen & Schuster (2010), Nissen & Schuster (2011), and Reggiani et al. (2017). Filled symbols are for kinematically-selected Gaia-Enceladus stars among the comparison.

The other stars in NS10 and R17 allow us to compare Sequoia stars with in situ (hot thick disk) stars and other typical halo stars. The high- α population in NS10 are considered to be stars that formed in situ; they are likely to have formed in the Milky Way and to have later heated onto the halo-like orbits. We simply call these stars “in situ stars” in what follows. The origin of R17 stars and NS10’s low- α stars that do not satisfy the Gaia-Enceladus selection is less clear. They are either Gaia-Enceladus stars, in situ stars, or stars from accreted galaxies other than Gaia-Enceladus. As there are no strong kinematic selections in NS10 and in R17, we consider these stars as typical halo stars.

We here compare chemical abundances of kinematically selected Sequoia stars, NS10 and R17 stars. We start the comparison with $[Mg/Fe]$ in Figure 5 since NS10 used this abundance ratio to separate high- and low- α populations. The majority of Sequoia stars do not follow the sequence formed by Gaia-Enceladus and they have lower $[Mg/Fe]$ ratios than Gaia-Enceladus stars at the same metallicity. A similar difference between Sequoia and Gaia-Enceladus stars is also found for Na (Figure 6) and some α elements (Figure 7). It is hard to see the difference in elemental abundances near the iron peak, except for Zn (Figure 8). One of the neutron capture elements, Y, also shows a different behavior between Sequoia and Gaia-Enceladus stars (Figure 9).

In summary, although a few objects that are kinematically selected as part of Sequoia at high metallicity (2657_5888 and HIP98492) seem to follow the trend of Gaia-Enceladus, there are clearly differences between the majority of Sequoia stars

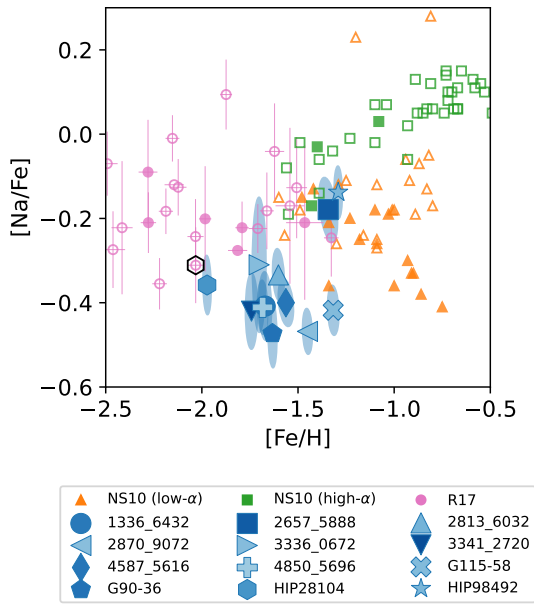


Fig. 6. Na abundances of the stars. Symbols are the same as those provided in Figure 5.

and Gaia-Enceladus stars in $[\text{Mg}/\text{Fe}]$, $[\text{Na}/\text{Fe}]$, $[\text{Ca}/\text{Fe}]$, $[\text{Ti}/\text{Fe}]$, $[\text{Zn}/\text{Fe}]$, and $[\text{Y}/\text{Fe}]$. Our homogeneously derived high-precision chemical abundances robustly confirm the finding of Matsuno et al. (2019) in Na, Mg, and Ca; Monty et al. (2020) in Mg and Ca; and Aguado et al. (2021) in the overall α -element abundance.

In order to quantify these differences, we followed the approach of Nissen & Schuster (2011) (see top panel of Figure 10). We first fit the abundance trend of Gaia-Enceladus in $[\text{X}/\text{Fe}]$ – $[\text{Fe}/\text{H}]$ with a quadratic polynomial using the kinematically selected stars and calculate the residual scatter (σ_{resid}). For each of the eight Sequoia stars in the metallicity range $-1.8 < [\text{Fe}/\text{H}] < -1.4$, we computed the deviation from this fit ($\Delta_{\text{Seq-GE}}$). We then computed $\chi^2 = \sum \Delta_{\text{Seq-GE}}^2 / (\sigma_{\text{resid}}^2 + \sigma^2([\text{X}/\text{Fe}]))$ and conducted a χ^2 test to obtain the probability that a χ^2 distribution with the degree of freedom of eight has a χ^2 higher than the observed value. This is to test if we can explain the displacement in abundance ratios of Sequoia stars from the trend of Gaia-Enceladus stars with the residual in the fit and the measurement uncertainties.

We also computed the abundance difference between Gaia-Enceladus and in situ stars ($\Delta_{\text{GE-in-situ}}$) at $-1.1 < [\text{Fe}/\text{H}] < -0.8$ by fitting the abundance trend of in situ stars in the same way. This calculation basically provides a similar quantity as Table 5 of Nissen & Schuster (2011). A difference to Nissen & Schuster (2011) is that here we compare kinematically selected Gaia-Enceladus stars instead of the low- α population with in situ stars (high- α population).

The results are summarized in Table 6. The average abundance difference between Gaia-Enceladus and Sequoia is largest in $[\text{Na}/\text{Fe}]$ (Figure 6), which is followed by $[\text{Mg}/\text{Fe}]$ (Figure 5). The differences in these abundance ratios are ~ 0.2 dex and highly significant. Other α elements, Ca and Ti, show differences of ~ 0.1 dex in $[\text{X}/\text{Fe}]$, while the difference in $[\text{Si}/\text{Fe}]$ is not as large as the other α elements (see Figure 7). Although the results of the χ^2 tests are significant for all of Si, Ca, and Ti, the large χ^2 in $[\text{Si}/\text{Fe}]$ might not be due to the average abundance difference between Sequoia and Gaia-Enceladus, but to the large spread in $[\text{Si}/\text{Fe}]$ ratios in our Sequoia stars. Given that we had to rely on

one or a few weak Si lines for its abundance determination, the $[\text{Si}/\text{Fe}]$ distribution needs to be taken with a caution.

These α -element abundance differences between Sequoia and Gaia-Enceladus are quite similar to those found by Nissen & Schuster (2011) between their low- α and high- α populations, which are still seen when we compare Gaia-Enceladus and the high- α in situ population (Table 6). Even though the differences are found at a different metallicity, this indicates that the same physical mechanism, specifically type Ia supernovae (SNe Ia) in this case, is likely responsible for creating the abundance differences. We discuss this further in Section 5.

Iron-group elements including Cr, Mn, and Ni do not show a significant abundance difference between Sequoia and Gaia-Enceladus (see Figure 8), although there is clearly a difference in $[\text{Ni}/\text{Fe}]$ between Gaia-Enceladus and in situ stars (Table 6; Nissen & Schuster 2011). The Ni abundance difference between Sequoia and Gaia-Enceladus is $\Delta[\text{Ni}/\text{Fe}] \sim 0.04$ dex if present. On the other hand, there is a statistically significant difference in $[\text{Zn}/\text{Fe}]$ by ~ 0.11 dex between Sequoia and Gaia-Enceladus (Table 6). Zinc also shows abundance differences between Gaia-Enceladus and in situ stars.

Neutron capture elements (Y and Ba) show relatively large scatters compared to other elements (Figure 9, see also Table 6). Despite the large scatter, $[\text{Y}/\text{Fe}]$ is significantly smaller for Sequoia stars than for Gaia-Enceladus stars (Table 6). Furthermore, Y is another element that shows an abundance difference in $[\text{X}/\text{Fe}]$ between Gaia-Enceladus and in situ stars.

We finally mention the relation between kinematics and chemical abundances within Sequoia. In Figures 5–9, the orbital energy of the stars are indicated by the intensity of the color. We did not find any significant correlations between kinematics and chemical abundances among Sequoia stars. We conducted t tests for the hypothesis that Sequoia stars, having high energy ($E > 1.2 \times 10^5 \text{ km}^2 \text{ s}^{-2}$), have the same $[\text{X}/\text{Fe}]$ as lower energy Sequoia stars at the metallicity range of $-1.8 < [\text{Fe}/\text{H}] < -1.4$. In all species, we cannot reject the hypothesis at more than a 2σ level, indicating that there are no significant abundance differences between Sequoia stars at a high energy and at a low energy.

5. Discussion

5.1. Chemical enrichments in Sequoia

The majority of the kinematically selected Sequoia stars that we have studied seem to show a different chemical abundance than Gaia-Enceladus, indicating that their progenitor is indeed different from Gaia-Enceladus. There are also a few stars that seem to have a chemical abundance comparable to Gaia-Enceladus. Although they could be stars stripped in the early phase of the Gaia-Enceladus accretion, as suggested by Koppelman et al. (2019), they do not seem to be a dominant population among stars having large retrograde motion and small binding energy. In the next section, we discuss which stars are likely true members of Sequoia from the point of chemical abundance.

In this section, we focus on the majority of stars having a different abundance pattern than Gaia-Enceladus and we further discuss the origin of the chemical signature of Sequoia. Sequoia stars tend to show lower $[\text{X}/\text{Fe}]$ in the same elements that show deficiency in Gaia-Enceladus in comparison to the in situ stars at high metallicity. We visualize this similarity in Figure 10, where the mean abundance difference between Sequoia and Gaia-Enceladus stars at $-1.8 < [\text{Fe}/\text{H}] < -1.4$ ($\langle \Delta_{\text{Seq-GE}} \rangle$) from Table 6 is plotted. The error bar reflects the standard de-

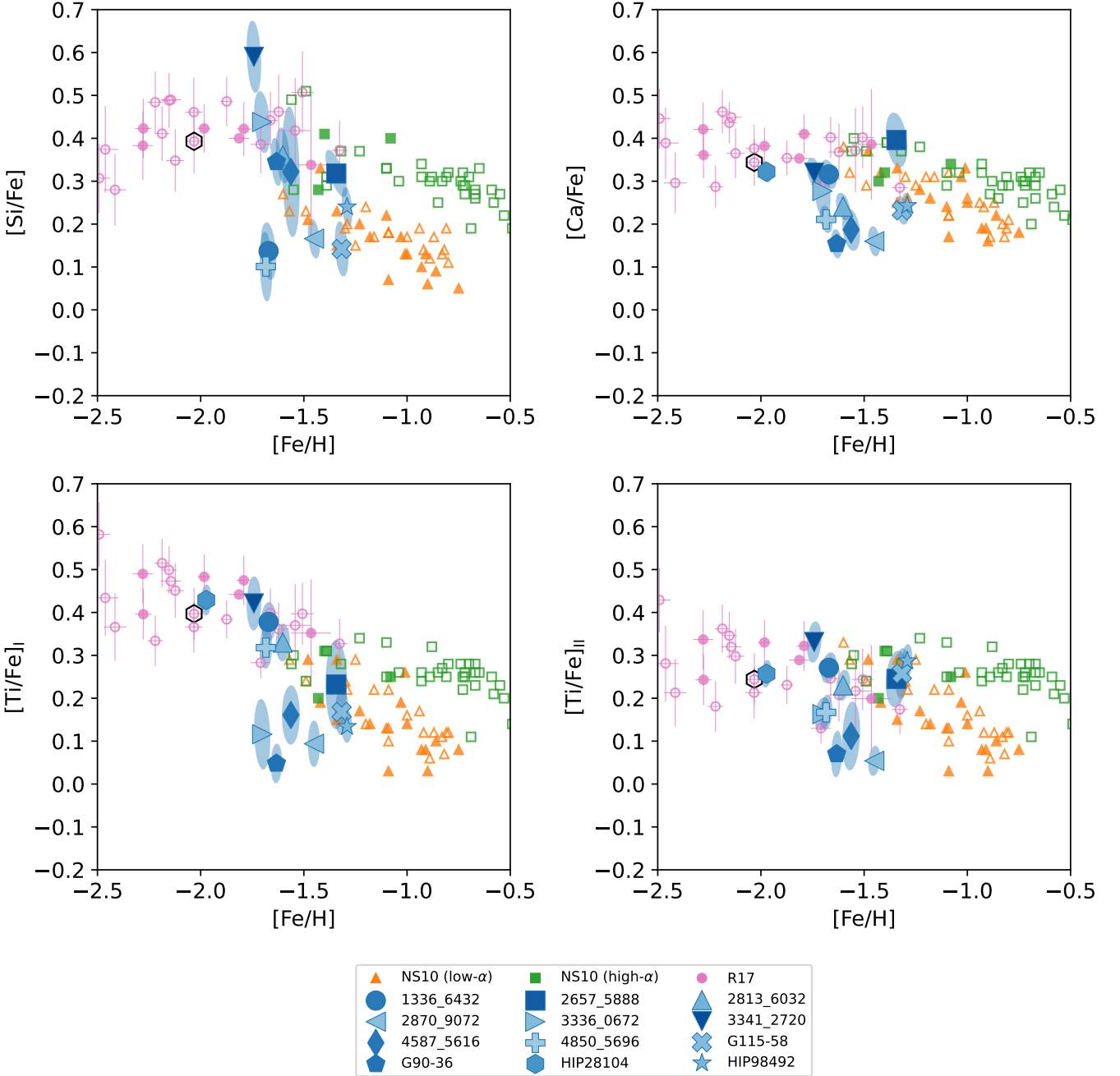


Fig. 7. Abundances of α -elements of the stars. Symbols are the same as those provided in Figure 5.

variation in $[X/Fe]$ in Sequoia. We also plotted the mean abundance difference between Gaia-Enceladus and in situ stars at $-1.1 < [Fe/H] < -0.8$ ($\langle \Delta_{GE-in-situ} \rangle$).

Figure 10 demonstrates a remarkable similarity between the patterns in $\langle \Delta_{Seq-GE} \rangle$ and $\langle \Delta_{GE-in-situ} \rangle$. We find the largest differences for Na and Mg, and mild differences for Ca, Ti, Zn, and Y in both comparisons. Although $\langle \Delta_{GE-in-situ} \rangle$ is clearly nonzero and negative in Si and Ni, it is hard to see a similar feature in $\langle \Delta_{Seq-GE} \rangle$ for these elements. The lack of difference in the Si abundance comparison between Sequoia and Gaia-Enceladus could be due to our larger measurement uncertainty and smaller number of stars compared to NS10 and Nissen &

Schuster (2011). In addition, Cr and Mn do not show significant differences in both comparisons.

The similarity in $\langle \Delta_{Seq-GE} \rangle$ and $\langle \Delta_{GE-in-situ} \rangle$ could suggest that the same physical process is responsible for shaping their patterns. The origin of the abundance difference between Gaia-Enceladus and in situ stars is usually attributed to chemical enrichment by SNe Ia; while in situ stars have not been significantly enriched by SNe Ia at $[Fe/H] \sim -1$ yet, Gaia-Enceladus has already been enriched by SNe Ia because of a longer star formation timescale, a lower star formation efficiency, and/or different star formation histories (e.g., Zolotov et al. 2010; Nissen & Schuster 2010, 2011; Fernández-Alvar et al. 2018; Gallart et al. 2019; Brook et al. 2020; Sanders et al. 2021), which would be

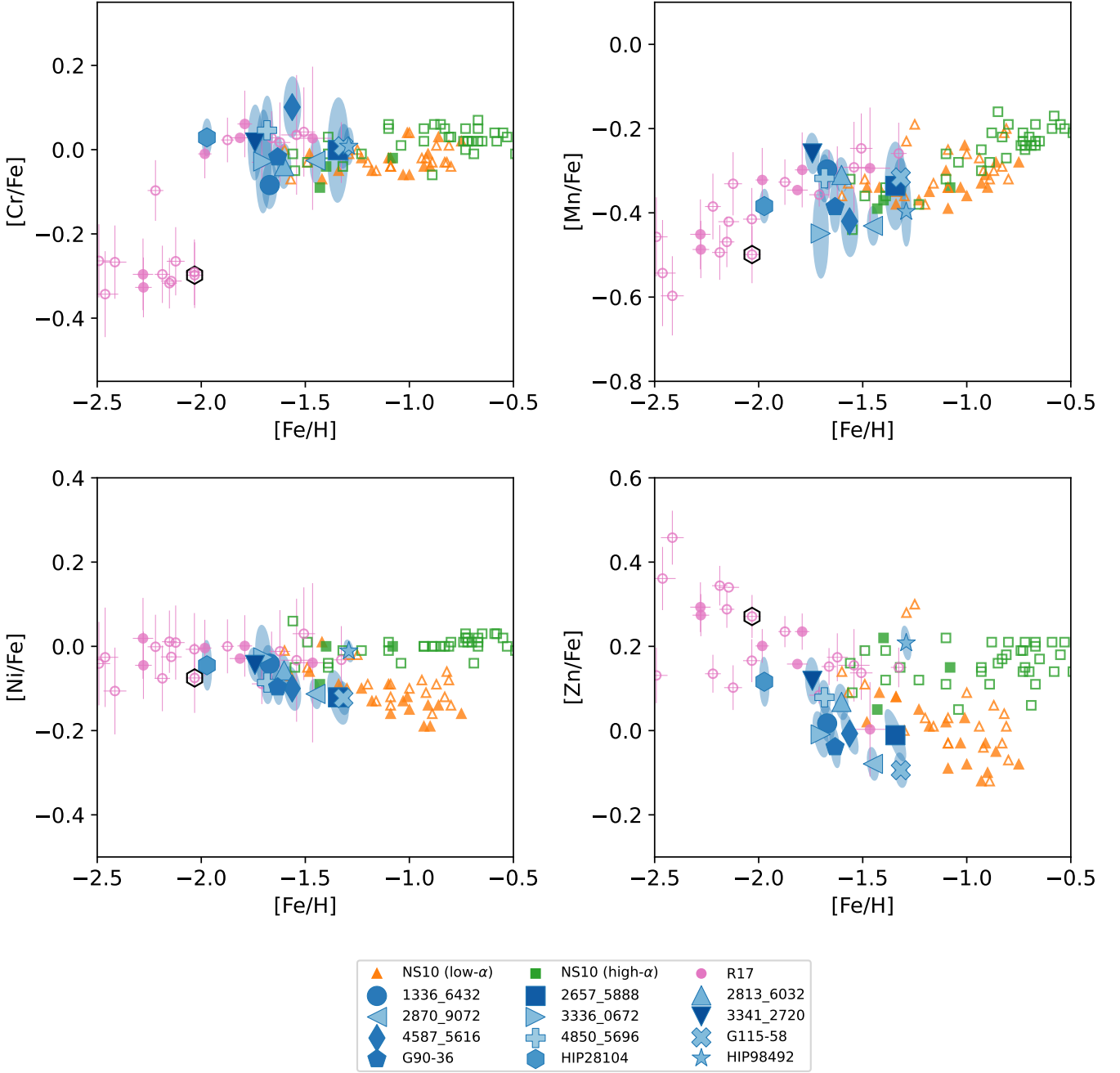


Fig. 8. Abundances of Cr, Mn, Ni, and Zn. Symbols are the same as those provided in Figure 5.

a consequence of the lower halo mass of Gaia-Enceladus than the main progenitor of the Milky Way. If we apply the same reasoning, the chemical abundance difference between Sequoia and Gaia-Enceladus is likely caused by larger SNe Ia enrichments in Sequoia at $[\text{Fe}/\text{H}] \sim -1.5$, which would indicate a lower mass for Sequoia than Gaia-Enceladus. This is consistent with the mass estimates from kinematic analysis, metallicity distribution, or a number count of stars (Koppelman et al. 2019; Myeong et al. 2019; Matsuno et al. 2019; Naidu et al. 2020).

Although $\langle \Delta_{\text{Seq-GE}} \rangle$ and $\langle \Delta_{\text{GE-in-situ}} \rangle$ show a remarkable overall similarity, one may notice a slight difference in Figure 10, especially in Ni. If the similarity in patterns in $\langle \Delta_{\text{Seq-GE}} \rangle$ and $\langle \Delta_{\text{GE-in-situ}} \rangle$ is primarily driven by the chemical enrichment from

SNe Ia, the lack of a Ni abundance difference between Sequoia and Gaia-Enceladus might indicate a variation in the properties of SNe Ia with, for example, environments or metallicity. For instance, Kirby et al. (2019) and Sanders et al. (2021) used a Ni abundance to conclude that the explosion of sub-Chandrasekhar mass is the dominant type of SNe Ia in dwarf galaxies and in Gaia-Enceladus. The evolution of a Ni abundance is actually sensitive to the explosion mechanism of a dominant type of SNe Ia (Palla 2021).

We note that, in addition to the larger contribution of SNe Ia, Fernández-Alvar et al. (2019) suggest a possibility of a top light initial mass function for Gaia-Enceladus by modeling α -element

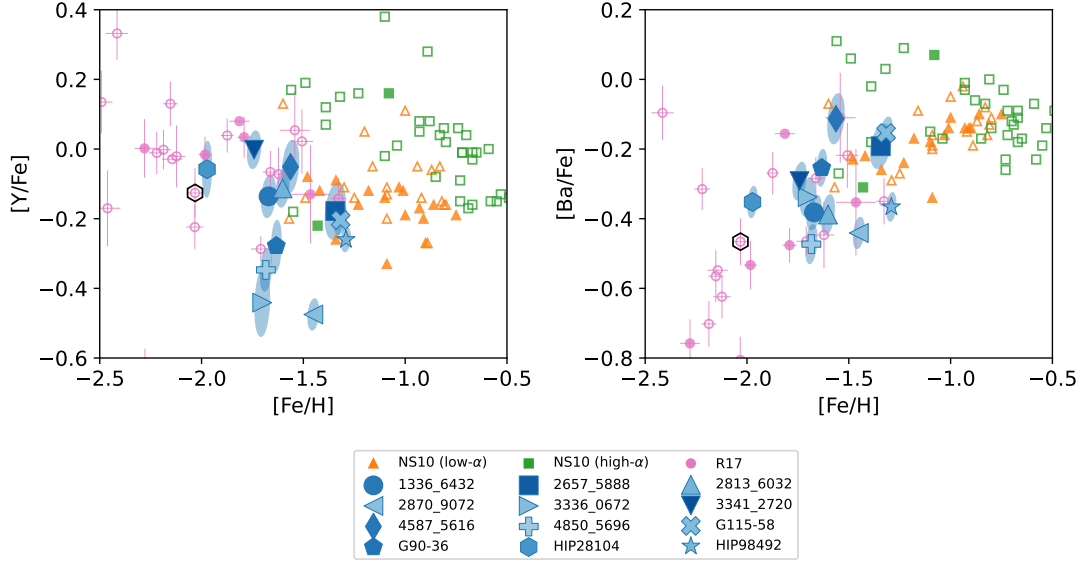


Fig. 9. Abundances of neutron-capture elements. Symbols are the same as those provided in Figure 5.

Table 6. Abundance difference between Sequoia and Gaia-Enceladus at $-1.8 < [\text{Fe}/\text{H}] < -1.4$, and that between Gaia-Enceladus and in situ stars at $-1.1 < [\text{Fe}/\text{H}] < -0.8$.

Species	$\Delta_{\text{Sequoia-GE}}$		$\sigma([\text{X}/\text{Fe}])$ Median	$\Delta_{\text{GE-in-situ}}$		p_{χ^2}
	Mean	Std.		Mean	Std.	
NaI	-0.223	0.055	0.073	-0.300	0.085	0.000
MgI	-0.195	0.040	0.040	-0.250	0.059	0.000
SiI	-0.037	0.146	0.068	-0.205	0.033	0.005
CaI	-0.123	0.054	0.033	-0.092	0.057	0.000
TiI	-0.113	0.119	0.050	-0.162	0.073	0.000
TiII	-0.096	0.080	0.038	-0.163	0.073	0.005
CrI	0.010	0.055	0.063	-0.039	0.035	0.843
MnI	-0.013	0.064	0.051	-0.053	0.040	0.552
NiI	-0.038	0.023	0.041	-0.147	0.026	0.725
ZnI	-0.114	0.049	0.045	-0.205	0.046	0.004
YII	-0.159	0.163	0.060	-0.265	0.073	0.000
BaII	-0.010	0.111	0.053	-0.106	0.076	0.258

abundances of halo stars from APOGEE. It remains to be seen if a similar explanation can be applied to Sequoia.

We now focus on neutron-capture elements, Y and Ba. While both elements are produced by the s process at solar metallicity, Y belongs to a group of light s -process elements. The weak s process, which operates in massive stars, contributes more to light s -process elements than the main s process in low-to-intermediate mass stars. In addition, the r process also significantly contributes to the enrichments of these elements in the early universe. Yttrium shows a relatively large scatter and a mild deficiency in Sequoia (Table 6). The Y deficiency seems to be driven by a few stars with low $[\text{Y}/\text{Fe}]$. They have $[\text{Y}/\text{Fe}] \sim -0.4$ and such a low abundance is hardly seen among Gaia-Enceladus stars in the NS10 and R17 samples. Barium also shows a large scatter, although the average abundance seems to be comparable to Gaia-Enceladus stars in the comparison samples.

To understand these trends, we plotted $[\text{Y}/\text{Ba}]$, $[\text{Y}/\text{Mg}]$, and $[\text{Ba}/\text{Mg}]$ abundances in Figure 11. The $[\text{Y}/\text{Ba}]$ ratio allowed us to infer the importance of a weak s process relative to the efficiency of Ba production either by low-to-intermediate mass stars

or by r -process nucleosynthesis. The $[\text{Y}/\text{Ba}]$ ratios of Sequoia stars tend to be lower than those of Gaia-Enceladus stars. The average difference between the two systems is -0.15 dex. Gaia-Enceladus is also known to possess low $[\text{Y}/\text{Ba}]$ values compared to in situ stars at $[\text{Fe}/\text{H}] \sim -1$ (Nissen & Schuster 2011).

The low $[\text{Y}/\text{Ba}]$ can be understood if the efficiency of the weak s process is lower in Sequoia, if low-to-intermediate mass stars in which the main- s process operates start to contribute to the chemical evolution of Sequoia, or if there are more r -process nucleosynthesis events in Sequoia that produce more Ba than Y. The abundance ratios $[\text{Y}/\text{Mg}]$ and $[\text{Ba}/\text{Mg}]$ displayed in the right two panels of Figure 11 further allowed us to infer the efficiency of the enrichment of the element X relative to the chemical enrichment by core-collapse supernovae (CCSNe) since CCSNe produce most of the Mg. Sequoia stars stand out less in $[\text{Y}/\text{Mg}]$, indicating that the production of Y is controlled by the abundance of Mg to some extent. This is expected if the majority of Y is produced by the weak s process, since its efficiency is dependent on CNO abundances (e.g., Prantzos et al. 1990), which are mostly produced by massive stars. A similar argument is applied to explain the Cu (and Y) abundance differences between

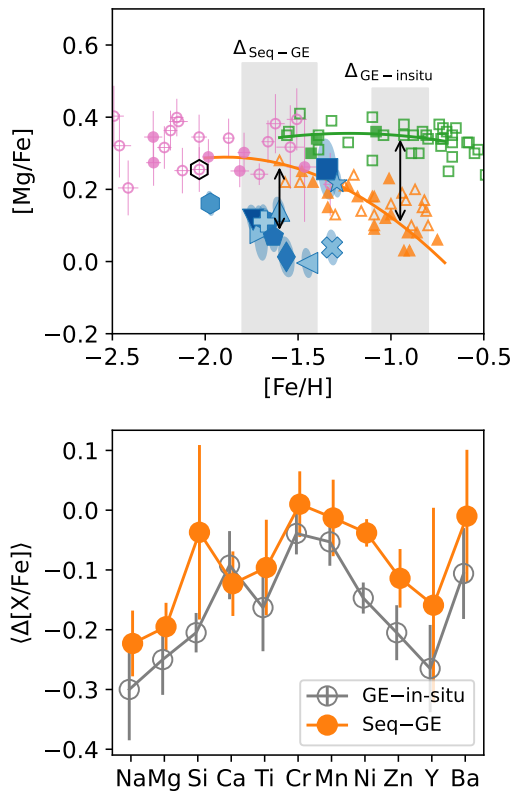


Fig. 10. Comparison of patterns in abundance difference. (Top:) Visualization of the calculations of $\Delta_{\text{Seq-GE}}$ and $\Delta_{\text{GE-in-situ}}$. See text for details. (Bottom:) Mean abundance difference between Sequoia and Gaia-Enceladus at $-1.8 < [\text{Fe}/\text{H}] < -1.4$, and that between Gaia-Enceladus and in situ stars at $-1.1 < [\text{Fe}/\text{H}] < -0.8$ ($\langle \Delta_{\text{Seq-GE}} \rangle$ and $\langle \Delta_{\text{GE-in-situ}} \rangle$). The error bar represents the standard deviation.

Gaia-Enceladus and in situ stars (Nissen & Schuster 2011; Matsuno et al. 2021a). Sequoia stars, on the other hand, are slightly enhanced in $[\text{Ba}/\text{Mg}]$, which might be related to the high Eu abundance reported by Aguado et al. (2021) and hence indicate efficient r -process nucleosynthesis in Sequoia.

While Y and Ba abundances provide some insights about the enrichment of neutron-capture elements in Sequoia, the information is still limited. It is highly desirable to measure abundances of many neutron-capture elements in future studies. For example, Aguado et al. (2021) suggest a possibility of enhanced r -process element abundance in Gaia-Enceladus and Sequoia from an Eu abundance, and Matsuno et al. (2021b) explain the high Eu abundance of Gaia-Enceladus as a combined effect of delay time in the r -process enrichment and the low star formation efficiency of Gaia-Enceladus. In a forthcoming paper, we plan to revisit weak and main s processes, and r -process enrichments in Sequoia with precise abundances of more neutron-capture elements (e.g., Sr, Eu).

There are some similarities in abundance ratios between Sequoia and the surviving dwarf galaxies around the Milky Way, such as Sagittarius, Fornax, Draco, Sculptor, Sextans dwarf spheroidal galaxies, and the Large and Small Magellanic Clouds (LMC and SMC). The Milky Way, Gaia-Enceladus, and many of the surviving dwarf galaxies show similarly super-solar $[\alpha/\text{Fe}]$ at low metallicity. However, since the “knee” metallicity ($[\text{Fe}/\text{H}]_{\text{knee}}$) at which systems start to show decreasing $[\alpha/\text{Fe}]$ with metallicity is below $[\text{Fe}/\text{H}] \lesssim -1.8$ in Fornax,

Draco, Sculptor, and Sextans dwarf galaxies, they show lower $[\alpha/\text{Fe}]$ than Gaia-Enceladus or the Milky Way in situ stars at $[\text{Fe}/\text{H}]_{\text{knee}} < [\text{Fe}/\text{H}]$ (Tolstoy et al. 2009; Cohen & Huang 2009; Kirby et al. 2011; Lemasle et al. 2012, 2014; Hendricks et al. 2014; Hill et al. 2019; Theler et al. 2020). Although the position of the knee is less clear in the LMC, SMC, and Sagittarius, they also show low α -element abundance at $[\text{Fe}/\text{H}] \sim -1.5$ (Nidever et al. 2020; Hasselquist et al. 2021). It is not clear if Sequoia shows a clear knee because of insufficient sampling of low-metallicity stars. Nonetheless, the abundance of the most metal-poor star in our sample (HIP28104) seems to support the existence of the knee at low metallicity.

5.2. Chemical identification of Sequoia members

Under the assumption that each system shows a well-defined track in $[\text{X}/\text{Fe}]-[\text{Fe}/\text{H}]$ planes and there are no chemical outliers, we should be able to chemically identify members of disrupted galaxies based on chemical abundance ratios. In this section, we try to separate individual Sequoia stars from Gaia-Enceladus ones solely based on the abundance ratios.

We first need to explore what is the best combination of elements to identify Sequoia stars. While considering the average of more elemental abundance ratios might lead to a reduced uncertainty, abundance differences might be smeared out if we add elements whose abundance does not show a difference between Sequoia and Gaia-Enceladus. We considered an average abundance of various combinations out of five elements (Na, Mg, Ca, Ti from Ti II, and Zn) since they show a clear abundance difference between Sequoia and Gaia-Enceladus in our study (Table 6). To quantitatively identify the best combination of elements, we followed the approach that is explained in Figure 10; we first fit the abundance trend of Gaia-Enceladus and then calculated χ^2 values for Sequoia stars in $-1.8 < [\text{Fe}/\text{H}] < -1.4$.

The χ^2 value was at its maximum when we considered the three elements, Na, Mg, and Ca (Figure 12). Therefore, we consider that the average of abundance ratios of $[\text{Na}/\text{Fe}]$, $[\text{Mg}/\text{Fe}]$, and $[\text{Ca}/\text{Fe}]$ offers a powerful diagnostic to chemically identify Sequoia stars. We note that the best combination of abundance ratios, however, varies depending on the data set, specifically the typical uncertainties in abundances of elements.

Among our sample, eight stars (1336_6432, 2813_6032, 2870_9072, 3341_2720, 4587_5616, 4850_5696, G115-58, and G90-36) deviate more than 2σ from the Gaia-Enceladus sequence in $\langle [\text{Na}/\text{Fe}], [\text{Mg}/\text{Fe}], [\text{Ca}/\text{Fe}] \rangle$, where σ is defined as $\Delta_{\text{Seq-GE}} / \sqrt{\sigma_{\text{resid}}^2 + \sigma^2(\langle [\text{X}/\text{Fe}] \rangle)}$. From the chemical point of view, these are the most likely members of Sequoia.

On the other hand, four stars do not deviate by more than 2σ . Two stars (2657_5888 and HIP98492) are at high metallicity and seem to be on the Gaia-Enceladus sequence. These stars might be those stripped in the very early stage of the Gaia-Enceladus accretion (Koppelman et al. 2019). The other two stars, 3336_0572 and HIP28104, have a relatively low metallicity. Since 3336_0572 is one of the stars for which the uncertainties in elemental abundances are large, the lack of significance might just reflect insufficient precision. HIP28104 has the lowest metallicity among our sample. Its metallicity might be too low even for the progenitor of Sequoia to be affected by SNe Ia.

Using these numbers, we could constrain the contribution of Sequoia stars and Gaia-Enceladus stars stripped early (Koppelman et al. 2019) among those selected to be highly retrograde. We found that two to four out of the 12 stars are from Gaia-Enceladus. Taking the Poisson error into account, we estimated

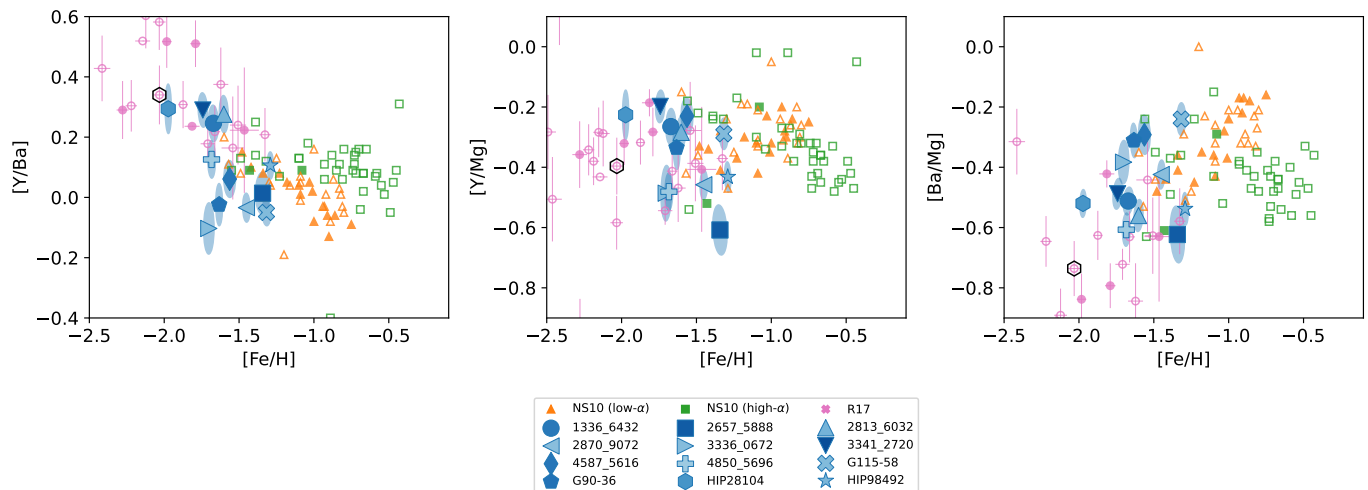


Fig. 11. Neutron-capture element abundances. Symbols are the same as those provided in Figure 5.

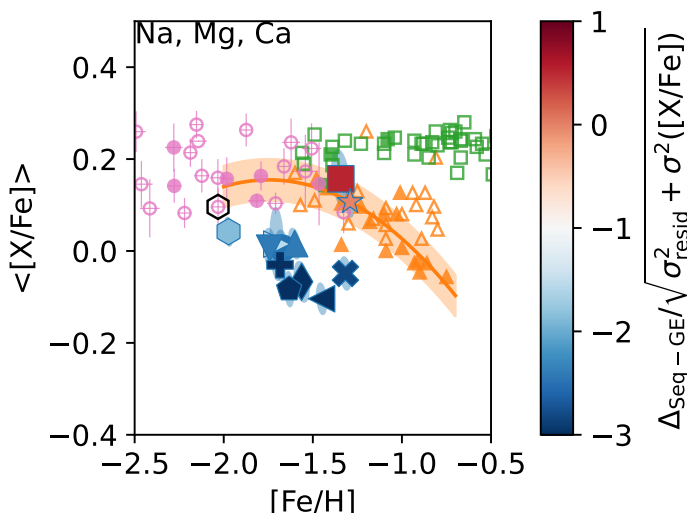


Fig. 12. Average values of $\langle [X/Fe] \rangle$ in Na, Mg, and Ca are plotted against $[Fe/H]$. For the calculation of the uncertainty in $\langle [X/Fe] \rangle$, we properly take correlated uncertainties between elemental abundances into account. Stars are color-coded according to the significance of their departure from the Gaia-Enceladus sequence, which is shown as the orange solid line. The Gaia-Enceladus sequence was obtained by fitting the abundance ratios of Gaia-Enceladus stars from Nissen & Schuster (2010) and Reggiani et al. (2017) with a quadratic polynomial. The residual scatter of Gaia-Enceladus around the fit is also shown around the fit.

that Gaia-Enceladus stars can contribute to 5-50 % of stars at large negative L_z and high E_n .

We now assess the minimum precision (σ_{obs}) required to separate individual Sequoia stars from Gaia-Enceladus using $[Mg/Fe]$ or $\langle [Na/Fe], [Mg/Fe], [Ca/Fe] \rangle$. The scatter among Sequoia stars (Table 6) and the residual scatter of Gaia-Enceladus stars from the fitting are comparable to the measurement uncertainty (~ 0.04 dex in both cases). Therefore, we consider that the dispersion in abundance ratios among Sequoia stars would be dominated by the measurement uncertainty, σ_{obs} . The difference between Sequoia and Gaia-Enceladus in these abundance ratios (Δ) are ~ 0.20 dex and ~ 0.18 dex, respectively. The required precision to chemically separate 84% of Sequoia stars with the

2σ criterion can be calculated by solving

$$|\Delta| - \sigma_{\text{obs}} > 2 \sqrt{\sigma_{\text{resid}}^2 + \sigma_{\text{obs}}^2}, \quad (4)$$

where the left side of the equation reflects the fact that about 84% of Sequoia stars have a larger deviation in abundance ratios from the Gaia-Enceladus trend than this value. Assuming $|\Delta| = 0.19$ and $\sigma_{\text{resid}} = 0.04$, we obtained $\sigma_{\text{obs}} \leq 0.07$ dex from this equation. This condition is met in our case even if we were to work only on Mg since the typical precision is $\sigma([Mg/Fe]) \sim 0.04$ dex. Considering more elemental abundance might help in some cases, although the typical uncertainty does not significantly improve in our case when we considered the three elements (Na, Mg, and Ca). Here, we note that it is also important to consider correlations between abundances of the elements to correctly estimate the uncertainty for their average abundance.

On the other hand, it is much easier to detect the average difference in chemical abundance between Sequoia and Gaia-Enceladus stars. The uncertainty of the mean is scaled with \sqrt{N} when systematic uncertainty can be neglected. Therefore, even if the observational uncertainty is comparable to the abundance difference between Sequoia and Gaia-Enceladus, four stars would be sufficient to detect the average abundance difference if the sample does not contain chemical outliers or contaminants.

5.3. Sequoia stars in the literature and surveys

In this section, we compare our results with those seen in previous studies and in surveys. As we have discussed in Section 1, previous studies do not agree on the chemical properties of Sequoia (Matsuno et al. 2019; Koppelman et al. 2019; Monty et al. 2020; Aguado et al. 2021; Feuillet et al. 2020). We revisit this problem using the updated data from spectroscopic surveys and a similar kinematic selection as we used in the present study.

We selected Sequoia member candidates following that used in Koppelman et al. (2019). The upper limits on circularity and energy were changed to -0.35 from -0.40 and to $-0.9 \times 10^5 \text{ km}^2 \text{ s}^{-2}$ from $-1.0 \times 10^5 \text{ km}^2 \text{ s}^{-2}$ so that the selection covers the kinematic extent of the stars in the present study.

In Figure 13, we plotted Sequoia candidates from Stephens & Boesgaard (2002), Ishigaki et al. (2012), and Reggiani &

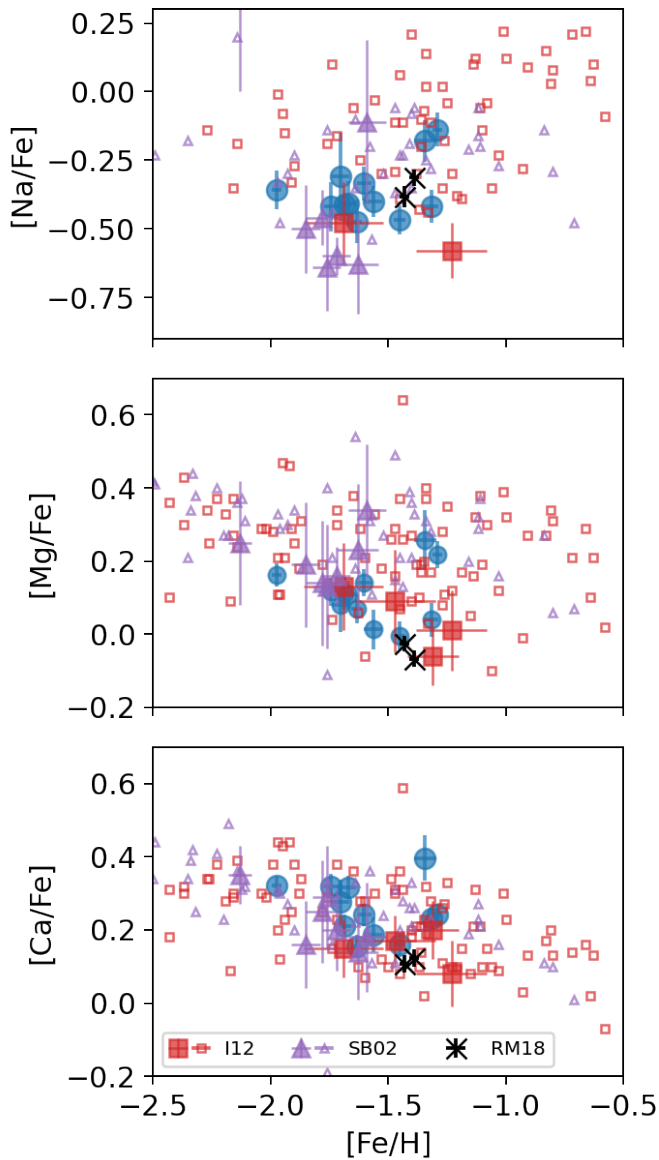


Fig. 13. Abundance of stars from the literature and from this study. The literature data come from Stephens & Boesgaard (2002, SB02), Ishigaki et al. (2012, I12), and Reggiani & Meléndez (2018, RM18). Sequoia stars are shown with filled symbols. Stars in the present study are shown with blue circles. We note that the uncertainty is shown with error bars instead of error ellipses for visualization.

Meléndez (2018), which contain more than one Sequoia candidate at $-2 < [\text{Fe}/\text{H}] < -1$. The abundance from Stephens & Boesgaard (2002) was updated following Monty et al. (2020). There are nine stars from Stephens & Boesgaard (2002) that satisfy the kinematic selection for Sequoia, of which six are at $-2 < [\text{Fe}/\text{H}] < -1$. The median reported uncertainty in $[\text{Mg}/\text{Fe}]$ is 0.17 dex, and hence it is difficult to chemically separate individual Sequoia stars (Section 5.2). However, it is still possible to detect the average difference; this is why Venn et al. (2004) were able to conclude that the most retrograde stars have a lower $[\text{Mg}/\text{Fe}]$. The situation with Ishigaki et al. (2012) is similar to that of Stephens & Boesgaard (2002) since the median uncertainty is 0.11 dex and the number of Sequoia stars is five (four in $-2 < [\text{Fe}/\text{H}] < -1$).

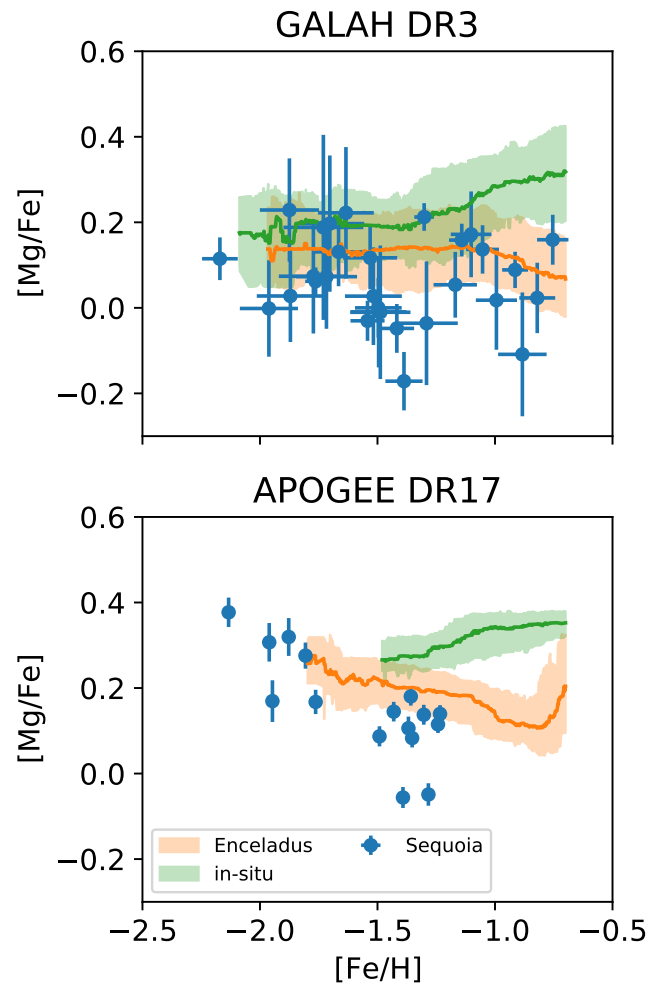


Fig. 14. Mg abundances of Sequoia, in situ stars, and Enceladus stars from GALAH DR3 and APOGEE DR17. The abundances of in situ stars and Enceladus stars are shown with a running median with a bin size of 0.1 dex. The shaded regions show the 16-84 percentile region.

On the other hand, Reggiani & Meléndez (2018) conducted a very high precision abundance analysis for a pair of HD134439 and HD134440 stars (e.g., $\sigma([\text{Mg}/\text{Fe}]) \sim 0.02$). With this precision, they are able to conclude that these two stars have a lower $[\alpha/\text{Fe}]$ than the low- α population from NS10.

Figure 14 shows the Mg abundance of Sequoia candidates from GALAH DR3 and APOGEE DR17. We selected APOGEE stars with $\text{ASPCAPFLAG} = 0$, $\text{STARFLAG} = 0$, $\text{TEFF} < 5500$, $\text{LOGG} < 3.5$, $\text{FE_H_FLAG} = 0$, and $\text{MG_FE_FLAG} = 0$. We also removed the known calibration cluster members and probable stellar cluster members. For GALAH DR3, we selected stars with $\text{teff} < 5500$, $\text{logg} < 3.5$, $\text{flag_fe_h} = 0$, and $\text{flag_mg_fe} = 0$. We selected in situ stars and Gaia-Enceladus stars following Matsuno et al. (2021b) and computed the running median and 16 and 84 percentiles of $[\text{Mg}/\text{Fe}]$ as a function of $[\text{Fe}/\text{H}]$ using a 0.1 dex bin size. We note that APOGEE yields a smaller uncertainty at this metallicity simply because their targets are brighter and the target S/N is higher than GALAH.

In both surveys, Sequoia stars clearly have a lower $[\text{Mg}/\text{Fe}]$ than Gaia-Enceladus (Figure 14), reproducing our own finding, although the absolute values of $[\text{Mg}/\text{Fe}]$ are different because of different approaches for abundance calculation and/or stellar pa-

parameter determination, for instance. The low abundance of Mg for Sequoia was not clearly seen in previous studies (e.g., Koppelman et al. 2019; Myeong et al. 2019; Feuillet et al. 2021), even though these authors used APOGEE data. This is likely because of different selection criteria and the sample size. The selection we made in the $L_z - E_n$ space allows for a smaller contamination compared to normalized action selections adopted in Myeong et al. (2019) and Feuillet et al. (2021) which includes low- E_n stars⁶. In order to deposit stars to a wide orbital energy range, the progenitor needs to be much more massive (Koppelman et al. 2019), which does not seem to be the case for Sequoia. The sample size with reliable abundance and reliable astrometric measurements has increased compared to more recent data releases from Gaia and APOGEE.

We also see an abundance difference in other elements including Al (APOGEE) and K (GALAH). However, a detailed investigation of Sequoia stars in large surveys is beyond the scope of the present study and is reserved for future studies.

We finally note that both surveys seem to cover a wider metallicity range than the present study. The narrow metallicity range of our study could be due to the metallicity cut at $[\text{Fe}/\text{H}] < -1$ for stars from LAMOST and the removal of two Sequoia candidates at a low metallicity as described in Section 2.

6. Conclusion

Through a differential abundance analysis of high-S/N and high-resolution spectra, we have shown that Sequoia stars are chemically distinguishable from Gaia-Enceladus. The eight Sequoia stars in the metallicity range of $-1.8 < [\text{Fe}/\text{H}] < -1.4$ have a lower $[\text{Na}/\text{Fe}]$, $[\text{Mg}/\text{Fe}]$, $[\text{Ca}/\text{Fe}]$, $[\text{Ti}/\text{Fe}]$, $[\text{Zn}/\text{Fe}]$, and $[\text{Y}/\text{Fe}]$ compared to the values expected for Gaia-Enceladus. The abundance difference is ~ 0.2 dex in $[\text{Na}/\text{Fe}]$ and in $[\text{Mg}/\text{Fe}]$ and ~ 0.1 dex in other abundance ratios. This pattern in the abundance difference is similar to that between Gaia-Enceladus and in situ stars at a higher metallicity. This suggests that Sequoia started experiencing chemical enrichment from SNe Ia at a lower metallicity than Gaia-Enceladus. We, however, note that we do not see a significant difference between Sequoia and Gaia-Enceladus in Ni abundance unlike in the comparison between Gaia-Enceladus and in situ stars, which might suggest that dominant types of SNe Ia are different between Sequoia and Gaia-Enceladus.

We have also shown that Sequoia stars show low $[\text{Y}/\text{Ba}]$ ratios, although its cause remains unclear. We will provide abundances for additional neutron-capture elements (e.g., Sr and Eu) in a future study to separate the contribution of a weak s process, main s process, and r process.

We have further shown that separation in Sequoia and Gaia-Enceladus becomes most prominent when we take the average of $[\text{Na}/\text{Fe}]$, $[\text{Mg}/\text{Fe}]$, and $[\text{Ca}/\text{Fe}]$, although this choice could vary depending on the data set. We have shown that individual Sequoia stars can be chemically separated if the abundance precision in $[\text{X}/\text{Fe}]$ is better than 0.07 dex. On the contrary, detecting the average abundance difference is much easier since the uncertainty on the mean scales with the square root of the number of stars if a kinematic selection that minimizes the contamination is adopted, and if there are few contaminants and chemical outliers.

⁶ The normalized action space is a space defined by J_ϕ/J_{tot} and $(J_z - J_R)/J_{\text{tot}}$, where J_ϕ , J_z , and J_R are the azimuthal, vertical, and radial actions, respectively, and $J_{\text{tot}} = |J_\phi| + J_z + J_R$. Although a selection in this normalized action space includes both stars at high E_n and low E_n , it should in principle be possible to make an action-based selection that is equivalent to the $L_z - E_n$ selection.

Using the average of $[\text{Na}/\text{Fe}]$, $[\text{Mg}/\text{Fe}]$, and $[\text{Ca}/\text{Fe}]$, we have concluded that eight out of the 12 stars we studied have distinct chemical abundances compared to Gaia-Enceladus. These eight stars are most likely true members of Sequoia. Only two of the remaining four stars seem to be contaminants from Gaia-Enceladus, indicating that the kinematic selection we adopted efficiently selects Sequoia stars. For the remaining two stars, it is not clear if they have the same chemical abundance as the other Sequoia stars or if they are contaminants from Gaia-Enceladus because of their low metallicity and/or insufficient precision in our abundance measurements.

We have demonstrated that we can see kinematically selected Sequoia stars having lower Na, Mg, and Ca abundances also in data from the literature (Stephens & Boesgaard 2002; Ishigaki et al. 2012; Reggiani & Meléndez 2018). Reggiani & Meléndez (2018) provide a sufficiently precise chemical abundance for the pair of HD134439 and HD134440 to chemically associate them to Sequoia. We also confirmed low Mg abundances of Sequoia stars using GALAH DR3 and APOGEE DR17.

Now that we have established the chemical distinctness of Sequoia from the major populations in the halo, namely Gaia-Enceladus and in situ stars, future studies of chemical abundances of Sequoia stars using large spectroscopic surveys are obvious next steps. A large sample is necessary to study if the group of stars referred to as Sequoia in the present study can be further separated into a few subgroups (Naidu et al. 2020; Lövdal et al. 2022; Ruiz-Lara et al. 2022). It would also be of interest to study the kinematic extent of chemically selected Sequoia stars. Large surveys that measure the chemical abundance of stars with a high-precision are necessary for these studies.

Acknowledgements. We thank Henriette Reggiani for providing the data that allow us to compare our results of equivalent width measurements and for checking their results in detail. We also thank Xiaodi Yu and Ian Roederer for taking the high-resolution spectrum with MIKE on Magellan. Poul Erik Nissen provided useful comments, which prompted us to conduct an additional validation of our results. We also thank the review made by the anonymous referee, which has improved the clarity of the manuscript. This research has been supported by a Spinoza Grant from the Dutch Research Council (NWO). WA, MNI, and TS were supported by JSPS KAKENHI Grant Number 21H04499. This research is based in part on data collected at Subaru Telescope, which is operated by the National Astronomical Observatory of Japan. We are honored and grateful for the opportunity of observing the Universe from Maunakea, which has the cultural, historical and natural significance in Hawaii. This research has made use of the Keck Observatory Archive (KOA), which is operated by the W. M. Keck Observatory and the NASA Exoplanet Science Institute (NExSci), under contract with the National Aeronautics and Space Administration. Part of the data were retrieved from the JVO portal (<http://jvo.nao.ac.jp/portal/>) operated by ADC/NAOJ. This work is partly based on data obtained from the ESO Science Archive Facility, which are based on observations collected at the European Organisation for Astronomical Research in the Southern Hemisphere under ESO programmes 67.D-0086(A), 95.D-0504(A), 095.D-0504(A).

References

- Aguado, D. S., Belokurov, V., Myeong, G. C., et al. 2021, *ApJ*, 908, L8
 Andrae, R. 2010, arXiv e-prints, arXiv:1009.2755
 Antoja, T., Ramos, P., Mateu, C., et al. 2020, *A&A*, 635, L3
 Belokurov, V., Erkal, D., Evans, N. W., Koposov, S. E., & Deason, A. J. 2018, *MNRAS*, 478, 611
 Belokurov, V., Sanders, J. L., Fattahi, A., et al. 2020, *MNRAS*, 494, 3880
 Belokurov, V., Zucker, D. B., Evans, N. W., et al. 2006, *ApJ*, 642, L137
 Bennett, M. & Bovy, J. 2019, *MNRAS*, 482, 1417
 Bernard, E. J., Ferguson, A. M. N., Schlafly, E. F., et al. 2016, *MNRAS*, 463, 1759
 Bernstein, R., Shectman, S. A., Gunnels, S. M., Mochnacki, S., & Athey, A. E. 2003, in *Society of Photo-Optical Instrumentation Engineers (SPIE) Conference Series*, Vol. 4841, *Instrument Design and Performance for Optical/Infrared Ground-based Telescopes*, ed. M. Iye & A. F. M. Moorwood, 1694–1704

- Brook, C. B., Kawata, D., Gibson, B. K., Gallart, C., & Vicente, A. 2020, *MNRAS*, 495, 2645
- Casagrande, L., Lin, J., Rains, A. D., et al. 2021, *MNRAS*, 507, 2684
- Casagrande, L. & VandenBerg, D. A. 2018, *MNRAS*, 479, L102
- Cayrel, R. 1988, in *The Impact of Very High S/N Spectroscopy on Stellar Physics*, ed. G. Cayrel de Strobel & M. Spite, Vol. 132, 345
- Chen, M. C., Herwig, F., Denissenkov, P. A., & Paxton, B. 2014, *MNRAS*, 440, 1274
- Chen, Y. Q. & Zhao, G. 2006, *MNRAS*, 370, 2091
- Cohen, J. G., Christlieb, N., Thompson, I., et al. 2013, *ApJ*, 778, 56
- Cohen, J. G. & Huang, W. 2009, *ApJ*, 701, 1053
- Dekker, H., D'Odorico, S., Kaufer, A., Delabre, B., & Kotzłowski, H. 2000, in *Society of Photo-Optical Instrumentation Engineers (SPIE) Conference Series*, Vol. 4008, *Optical and IR Telescope Instrumentation and Detectors*, ed. M. Iye & A. F. Moorwood, 534–545
- Di Matteo, P., Haywood, M., Lehnert, M. D., et al. 2019, *A&A*, 632, A4
- Fernández-Alvar, E., Carigi, L., Schuster, W. J., et al. 2018, *ApJ*, 852, 50
- Fernández-Alvar, E., Fernández-Trincado, J. G., Moreno, E., et al. 2019, *MNRAS*, 487, 1462
- Feuillet, D. K., Feltzing, S., Sahlholdt, C. L., & Casagrande, L. 2020, *MNRAS*, 497, 109
- Feuillet, D. K., Sahlholdt, C. L., Feltzing, S., & Casagrande, L. 2021, *MNRAS*, 508, 1489
- Foreman-Mackey, D., Hogg, D. W., Lang, D., & Goodman, J. 2013, *PASP*, 125, 306
- Gaia Collaboration, Brown, A. G. A., Vallenari, A., et al. 2018, *A&A*, 616, A1
- Gaia Collaboration, Prusti, T., de Bruijne, J. H. J., et al. 2016, *A&A*, 595, A1
- Gallart, C., Bernard, E. J., Brook, C. B., et al. 2019, *Nature Astronomy*, 3, 407
- Gratton, R. G., Carretta, E., Desidera, S., et al. 2003, *A&A*, 406, 131
- Green, G. M., Schlafly, E., Zucker, C., Speagle, J. S., & Finkbeiner, D. 2019, *ApJ*, 887, 93
- Grillmair, C. J. 2006, *ApJ*, 645, L37
- Gustafsson, B., Edvardsson, B., Eriksson, K., et al. 2008, *A&A*, 486, 951
- Hasselquist, S., Hayes, C. R., Lian, J., et al. 2021, arXiv e-prints, arXiv:2109.05130
- Haywood, M., Di Matteo, P., Lehnert, M. D., et al. 2018, *ApJ*, 863, 113
- Helmi, A., Babusiaux, C., Koppelman, H. H., et al. 2018, *Nature*, 563, 85
- Hendricks, B., Koch, A., Lanfranchi, G. A., et al. 2014, *ApJ*, 785, 102
- Hill, V., Skúladóttir, Á., Tolstoy, E., et al. 2019, *A&A*, 626, A15
- Ibata, R. A., Gilmore, G., & Irwin, M. J. 1994, *Nature*, 370, 194
- Ishigaki, M. N., Chiba, M., & Aoki, W. 2012, *ApJ*, 753, 64
- Ji, A. P., Li, T. S., Hansen, T. T., et al. 2020, *AJ*, 160, 181
- King, J. R. 1997, *AJ*, 113, 2302
- Kirby, E. N., Cohen, J. G., Smith, G. H., et al. 2011, *ApJ*, 727, 79
- Kirby, E. N., Xie, J. L., Guo, R., et al. 2019, *ApJ*, 881, 45
- Koppelman, H., Helmi, A., & Veljanoski, J. 2018, *ApJ*, 860, L11
- Koppelman, H. H., Helmi, A., Massari, D., Price-Whelan, A. M., & Starkenburg, T. K. 2019, *A&A*, 631, L9
- Kroupa, P. & Weidner, C. 2003, *ApJ*, 598, 1076
- Lallement, R., Babusiaux, C., Vergely, J. L., et al. 2019, *A&A*, 625, A135
- Lemasle, B., de Boer, T. J. L., Hill, V., et al. 2014, *A&A*, 572, A88
- Lemasle, B., Hill, V., Tolstoy, E., et al. 2012, *A&A*, 538, A100
- Lim, D., Koch-Hansen, A. J., Hansen, C. J., et al. 2021, *A&A*, 655, A26
- Lind, K., Asplund, M., Barklem, P. S., & Belyaev, A. K. 2011, *A&A*, 528, A103
- Lövdal, S. S., Ruiz-Lara, T., Koppelman, H. H., et al. 2022, arXiv e-prints, arXiv:2201.02404
- Mackereth, J. T., Schiavon, R. P., Pfeffer, J., et al. 2019, *MNRAS*, 482, 3426
- Malhan, K., Ibata, R. A., & Martin, N. F. 2018, *MNRAS*, 481, 3442
- Matsuno, T., Aoki, W., Casagrande, L., et al. 2021a, *ApJ*, 912, 72
- Matsuno, T., Aoki, W., & Suda, T. 2019, *ApJ*, 874, L35
- Matsuno, T., Hirai, Y., Tarumi, Y., et al. 2021b, *A&A*, 650, A110
- McMillan, P. J. 2017, *MNRAS*, 465, 76
- Monty, S., Venn, K. A., Lane, J. M. M., Lokhorst, D., & Yong, D. 2020, *MNRAS*, 497, 1236
- Myeong, G. C., Evans, N. W., Belokurov, V., Sanders, J. L., & Koposov, S. E. 2018, *ApJ*, 856, L26
- Myeong, G. C., Vasiliev, E., Iorio, G., Evans, N. W., & Belokurov, V. 2019, *MNRAS*, 488, 1235
- Naidu, R. P., Conroy, C., Bonaca, A., et al. 2020, *ApJ*, 901, 48
- Nidever, D. L., Hasselquist, S., Hayes, C. R., et al. 2020, *ApJ*, 895, 88
- Nissen, P. E. & Schuster, W. J. 1997, *A&A*, 326, 751
- Nissen, P. E. & Schuster, W. J. 2010, *A&A*, 511, L10
- Nissen, P. E. & Schuster, W. J. 2011, *A&A*, 530, A15
- Noguchi, K., Aoki, W., Kawanomoto, S., et al. 2002, *PASJ*, 54, 855
- O'Malley, E. M., McWilliam, A., Chaboyer, B., & Thompson, I. 2017, *ApJ*, 838, 90
- Palla, M. 2021, *MNRAS*, 503, 3216
- Prantzos, N., Hashimoto, M., & Nomoto, K. 1990, *A&A*, 234, 211
- Ramírez, I., Meléndez, J., Bean, J., et al. 2014, *A&A*, 572, A48
- Ramos, P., Mateu, C., Antoja, T., et al. 2020, *A&A*, 638, A104
- Reggiani, H. & Meléndez, J. 2018, *MNRAS*, 475, 3502
- Reggiani, H., Meléndez, J., Kobayashi, C., Karakas, A., & Placco, V. 2017, *A&A*, 608, A46
- Reid, M. J. & Brunthaler, A. 2004, *ApJ*, 616, 872
- Ruiz-Dern, L., Babusiaux, C., Arenou, F., Turon, C., & Lallement, R. 2018, *A&A*, 609, A116
- Ruiz-Lara, T., Matsuno, T., Sofie Lövdal, S., et al. 2022, arXiv e-prints, arXiv:2201.02405
- Sanders, J. L., Belokurov, V., & Man, K. T. F. 2021, *MNRAS*, 506, 4321
- Schönrich, R., Binney, J., & Dehnen, W. 2010, *MNRAS*, 403, 1829
- Snedden, C. 1973, *ApJ*, 184, 839
- Stephens, A. & Boesgaard, A. M. 2002, *AJ*, 123, 1647
- Suda, T., Hidaka, J., Aoki, W., et al. 2017, *PASJ*, 69, 76
- Suda, T., Katsuta, Y., Yamada, S., et al. 2008, *PASJ*, 60, 1159
- Suda, T., Yamada, S., Katsuta, Y., et al. 2011, *MNRAS*, 412, 843
- Tajitsu, A., Aoki, W., & Yamamuro, T. 2012, *PASJ*, 64, 77
- Theler, R., Jablonka, P., Lucchesi, R., et al. 2020, *A&A*, 642, A176
- Tolstoy, E., Hill, V., & Tosi, M. 2009, *ARA&A*, 47, 371
- Vasiliev, E. 2019, *MNRAS*, 482, 1525
- Venn, K. A., Irwin, M., Shetrone, M. D., et al. 2004, *AJ*, 128, 1177
- Vogt, S. S., Allen, S. L., Bigelow, B. C., et al. 1994, in *Proc. SPIE*, Vol. 2198, *Instrumentation in Astronomy VIII*, ed. D. L. Crawford & E. R. Craine, 362
- Yamada, S., Suda, T., Komiya, Y., Aoki, W., & Fujimoto, M. Y. 2013, *MNRAS*, 436, 1362
- Yuan, Z., Myeong, G. C., Beers, T. C., et al. 2020, *ApJ*, 891, 39
- Zolotov, A., Willman, B., Brooks, A. M., et al. 2010, *ApJ*, 721, 738

Table A.1. Abundances of Gaia EDR3 360456543361799808

	N	[X/H]	σ	[X/Fe]	σ
FeI	86	-1.809	0.032
FeII	14	-1.851	0.019
NaI	2	-2.027	0.092	-0.218	0.087
MgI	6	-1.588	0.039	0.221	0.039
SiI	1	-1.432	0.063	0.377	0.066
CaI	18	-1.414	0.032	0.395	0.032
TiI	12	-1.354	0.064	0.455	0.054
TiII	10	-1.442	0.033	0.410	0.030
CrI	2	-1.910	0.089	-0.101	0.083
MnI	2	-2.184	0.057	-0.375	0.048
NiI	11	-1.761	0.049	0.048	0.045
ZnI	2	-1.670	0.045	0.139	0.041
YII	2	-1.911	0.049	-0.060	0.046
BaII	3	-2.032	0.053	-0.181	0.049

Table B.1. Abundance difference due to different $\log g$

	2657_5888	4587_5696
$\Delta[\text{Fe}/\text{H}]_{\text{I}}$	-0.036	0.018
$\Delta[\text{Na}/\text{H}]_{\text{I}}$	0.089	-0.005
$\Delta[\text{Mg}/\text{H}]_{\text{I}}$	-0.050	-0.044
$\Delta[\text{Si}/\text{H}]_{\text{I}}$	0.058	0.076
$\Delta[\text{Ca}/\text{H}]_{\text{I}}$	-0.106	-0.071
$\Delta[\text{Ti}/\text{H}]_{\text{I}}$	-0.109	-0.016
$\Delta[\text{Cr}/\text{H}]_{\text{I}}$	-0.044	-0.040
$\Delta[\text{Mn}/\text{H}]_{\text{I}}$	-0.052	0.013
$\Delta[\text{Ni}/\text{H}]_{\text{I}}$	0.011	0.050
$\Delta[\text{Zn}/\text{H}]_{\text{I}}$	0.099	0.142
$\Delta[\text{Fe}/\text{H}]_{\text{II}}$	0.178	0.202
$\Delta[\text{Ti}/\text{H}]_{\text{II}}$	0.121	0.165
$\Delta[\text{Y}/\text{H}]_{\text{II}}$	0.149	0.200
$\Delta[\text{Ba}/\text{H}]_{\text{II}}$	0.113	0.154

Appendix A: Analysis of Gaia EDR3 360456543361799808

Gaia EDR3 360456543361799808 turned out not to belong to Sequoia after updating the radial velocity to -377.6 km s^{-1} using our high-resolution spectroscopy from the LAMOST DR4 value of $-288.15 \text{ km s}^{-1}$. With this updated radial velocity, we estimated $L_z = -841 \text{ kpc km s}^{-1}$ and $E_n = -1.580 \times 10^5 \text{ km}^2 \text{ s}^{-2}$. We note that LAMOST DR6 no longer provides a radial velocity for this object and Gaia DR2 gives -376.3 km s^{-1} , which is closer to our measurement from the high-resolution spectrum.

We still measured stellar parameters and abundances for this object. The derived stellar parameters are $T_{\text{eff}} = 6172 \pm 70 \text{ K}$, $\log g = 3.905 \pm 0.032$, $v_t = 1.567 \pm 0.108 \text{ km s}^{-1}$, and $[\text{Fe}/\text{H}] = -1.865 \pm 0.019$. The derived abundances are summarized in Table A.1. This star has a comparable abundance to Gaia-Enceladus and in situ stars.

Appendix B: Spectroscopic gravity for 2657_5888 and 4587_5696

The two stars, 2657_5888 and 4587_5696, are not on metal-poor isochrones (Figure 1) and have significantly different iron abundances from neutral and ionized species (Table D.1). We confirmed the offsets with different isochrones (BaSTI and MIST isochrones). These indicate that the Gaia EDR3 parallax and photometry might not be yielding correct $\log g$. An alternative method for the $\log g$ determination is by requiring ionization balance, namely by enforcing neutral and ionized iron lines to yield consistent abundances.

The $\log g$ values that realize ionization balance are 4.69 and 4.96 for 2657_5888 and 4587_5696, respectively. Table B.1 shows the difference between the abundances derived with these $\log g$ values and those obtained assuming parameters from Table 4.

The change in $\log g$ does not affect our conclusion. Although the difference shown in Table 4 is in [X/H], a smaller difference is usually found when the comparison is made in [X/Fe] since we used the Fe abundance derived from iron lines in the same ionization stage as the species X. Our conclusions are mostly based on [X/Fe]. In addition, these changes in $\log g$ affect only two stars, one of which was not regarded as chemically compatible with being a part of Sequoia.

Nonetheless, it is worthwhile mentioning how elemental abundances are affected. For example, the change in [X/Fe] is

negative in Mg, Ca, Ti I, Ti II, Y II, and Ba II; additionally, [Mg/Fe], [Ca/Fe], [Ti/Fe], [Y/Fe], and [Ba/Fe] of the two stars might be lower than shown in Figures 5, 7, and 9. On the other hand, [Si/Fe] and [Zn/Fe] ratios would be shifted higher if we adopted $\log g$ from the ionization balance. Effects on [X/Fe] of Cr, Mn, and Ni are minimal and the effect on [Na/Fe] is quite different between the two stars.

Possible reasons for the offset of the two stars on the color-magnitude diagram are as follows: i) they are parts of unresolved binaries; ii) their extinctions are under-estimated; iii) Gaia does not provide correct astrometry and/or photometry; and iv) they experienced spacial process by which their current positions on the color-magnitude diagram does not reflect their age and metallicity. Below, we discuss these four possibilities.

The first possibility seems most likely. Although there are no signatures of the presence of companions in our high-resolution spectra, it is possible that the maximum velocity difference is too small to see the binary signature in our high-resolution spectra (smaller than a few km s^{-1}) and, at the same time, the on-sky separation is smaller than what Gaia or photometric surveys can spatially resolve (less than a few tenths of an arcsec). In addition, there is a possibility that we are not seeing any signatures of binarity simply because the orbit is at the phase where the radial velocity difference between the components is small. Long-term monitoring of the variation in high-resolution spectra will be able to provide an answer to this. We also note that the ruwe value in Gaia EDR3, which can be significantly higher than one because of astrometric jitter caused by unresolved companions, is ~ 1.73 for 4587_5696, supporting this scenario.

We can rule out the second possibility since there is no sign of significant extinction in the high-resolution spectra in the form of Na I interstellar absorptions. We will be able to test the third possibility with improved astrometry and photometry from future Gaia data releases. If all the other scenarios do not hold with future Gaia data, we can then examine the fourth possibility.

Appendix C: Uncertainties in stellar parameters

Stellar parameters are dependent on each other and hence are determined iteratively. We, therefore, need to take the uncertainties in the other parameters into account when estimating the uncertainty in one parameter. We also consider correlations between stellar parameters and their effects on abundances. The goal of this section is to obtain the covariance matrix Σ among the four stellar parameters.

We consider four stellar parameters, $x_1 = T_{\text{eff}}$, $x_2 = \log g$, $x_3 = v_t$, and $x_4 = [\text{Fe}/\text{H}]_{\text{sp}}$. A parameter x_i was determined through a function $f_i(\mathbf{x})$; the set of best estimates $\tilde{\mathbf{x}}$ satisfies $\tilde{x}_i = f_i(\tilde{\mathbf{x}})$. We first estimated the uncertainty in each parameter ϵ_i by fixing other parameters as described in Section 3.2. The ϵ_i is not necessarily close to realistic uncertainty since it neglects the effect of the uncertainties in other parameters. The values we estimated can be expressed as

$$x_i = f_i(\mathbf{x}) + \epsilon_i, \quad (\text{C.1})$$

which can be approximated as

$$x_i \simeq f_i(\tilde{\mathbf{x}}) + \sum_{i \neq j} \frac{\partial f_i}{\partial x_j} (x_j - \tilde{x}_j) + \epsilon_i. \quad (\text{C.2})$$

Here we define $\delta \mathbf{x} = \mathbf{x} - \tilde{\mathbf{x}}$ and the matrix \mathbf{A} whose element is

$$A_{ij} = \begin{cases} 0 & (i = j) \\ \frac{\partial f_i}{\partial x_j} & (i \neq j). \end{cases} \quad (\text{C.3})$$

From equation C.1, we can write

$$\delta \mathbf{x} = \boldsymbol{\epsilon} + \mathbf{A} \delta \mathbf{x}, \quad (\text{C.4})$$

hence

$$(\mathbf{I} - \mathbf{A}) \delta \mathbf{x} = \boldsymbol{\epsilon}. \quad (\text{C.5})$$

Since $\Sigma = \langle \delta \mathbf{x} \delta \mathbf{x}^T \rangle$ and $\langle \epsilon_i, \epsilon_j \rangle = \delta_{ij} \epsilon_i^2$, the covariance matrix can be calculated from

$$\Sigma = (\mathbf{I} - \mathbf{A})^{-1} \text{diag}(\epsilon_i^2) [(\mathbf{I} - \mathbf{A})^{-1}]^T. \quad (\text{C.6})$$

The above calculation is equivalent to considering the following likelihood,

$$\mathcal{L} \propto \prod \exp\left[-\frac{1}{2} \frac{(x_i - f_i(\mathbf{x}))^2}{\epsilon_i^2}\right], \quad (\text{C.7})$$

and calculating Fisher's matrix \mathcal{F} , whose element is expressed as

$$\mathcal{F}_{lm} = -\frac{\partial^2 \log \mathcal{L}}{\partial x_l \partial x_m}. \quad (\text{C.8})$$

Assuming \mathbf{x} follows a multivariate Gaussian distribution, \mathcal{F} is equal to Σ^{-1} (e.g., Andrae 2010). Eq. C.6 can also be derived from this equation.

In practice, we estimated A_{ij} by redetermining the parameter i while shifting the parameter j by $\pm \epsilon_j$. Since we determined both T_{eff} and v_t from neutral Fe lines, the correlation between these two parameters can be significant.

Appendix D: Additional table

Table D.1. Abundances of Sequoia stars

1336_6432			2657_5888			2813_6032		
N	[X/H]	σ	N	[X/H]	σ	N	[X/H]	σ
FeI	-1.671	0.033	90	-1.343	0.048	97	-1.602	0.030
FeII	-1.692	0.027	9	-1.517	0.045	16	-1.632	0.026
NaI	-2.079	0.085	4	-1.522	0.071	4	-1.936	0.063
MgI	-1.563	0.039	2	-1.087	0.086	6	-1.461	0.037
SiI	-1.533	0.064	4	-1.025	0.035	1	-1.242	0.061
CaI	-1.354	0.034	13	-0.947	0.067	19	-1.361	0.032
TiI	-1.293	0.056	16	-1.110	0.113	10	-1.272	0.053
TiII	-1.421	0.035	8	-1.273	0.059	10	-1.403	0.034
CrI	-1.755	0.066	3	-1.343	0.134	3	-1.640	0.061
MnI	-1.968	0.055	2	-1.679	0.114	3	-1.912	0.048
NiI	-1.711	0.047	22	-1.464	0.057	15	-1.659	0.040
ZnI	-1.654	0.048	2	-1.354	0.039	2	-1.534	0.045
YII	-1.828	0.061	1	-1.695	0.062	1	-1.745	0.054
BaII	-2.074	0.052	3	-1.709	0.050	4	-2.021	0.057
2870_9072			3336_0672			3341_2720		
N	[X/H]	σ	N	[X/H]	σ	N	[X/H]	σ
FeI	-1.451	0.025	94	-1.702	0.035	79	-1.742	0.031
FeII	-1.438	0.024	16	-1.667	0.028	10	-1.822	0.029
NaI	-1.919	0.055	3	-2.012	0.163	2	-2.162	0.095
MgI	-1.455	0.039	7	-1.622	0.072	6	-1.626	0.040
SiI	-1.285	0.042	1	-1.264	0.068	1	-1.152	0.080
CaI	-1.291	0.035	20	-1.425	0.061	21	-1.422	0.035
TiI	-1.357	0.058	14	-1.586	0.082	9	-1.321	0.070
TiII	-1.384	0.038	9	-1.504	0.032	11	-1.492	0.051
CrI	-1.477	0.058	4	-1.730	0.127	2	-1.725	0.094
MnI	-1.882	0.050	4	-2.151	0.109	2	-2.001	0.055
NiI	-1.564	0.036	17	-1.728	0.076	4	-1.786	0.044
ZnI	-1.530	0.039	2	-1.710	0.048	2	-1.624	0.058
YII	-1.913	0.048	2	-2.108	0.092	2	-1.824	0.058
BaII	-1.879	0.050	4	-2.005	0.050	4	-2.114	0.061
4587_5616			4850_5696			G115-58		
N	[X/H]	σ	N	[X/H]	σ	N	[X/H]	σ
FeI	-1.563	0.039	98	-1.684	0.026	106	-1.317	0.029
FeII	-1.730	0.053	13	-1.708	0.027	18	-1.364	0.021
NaI	-1.964	0.058	3	-2.095	0.066	3	-1.736	0.062
MgI	-1.551	0.056	4	-1.574	0.047	5	-1.278	0.050
SiI	-1.242	0.147	1	-1.583	0.079	3	-1.175	0.060
CaI	-1.376	0.052	23	-1.473	0.032	19	-1.085	0.035
TiI	-1.403	0.079	10	-1.366	0.055	10	-1.149	0.062
TiII	-1.617	0.066	14	-1.540	0.037	9	-1.106	0.059
CrI	-1.463	0.082	6	-1.638	0.085	4	-1.309	0.060
MnI	-1.984	0.090	8	-2.002	0.061	3	-1.634	0.052

Table D.1. continued.

G90-36			HIP28104			HIP98492									
N	[X/H]	σ	N	[X/H]	σ	N	[X/H]	σ							
NiI	18	-1.663	0.053	-0.100	0.051	9	-1.770	0.052	-0.086	0.049	14	-1.440	0.043	-0.123	0.038
ZnI	2	-1.570	0.035	-0.007	0.048	2	-1.605	0.043	0.079	0.039	2	-1.411	0.044	-0.094	0.040
YII	2	-1.781	0.051	-0.051	0.075	1	-2.055	0.058	-0.347	0.060	2	-1.567	0.045	-0.204	0.041
BaII	4	-1.842	0.052	-0.113	0.071	4	-2.181	0.054	-0.473	0.055	4	-1.518	0.049	-0.154	0.045
G90-36			HIP28104			HIP98492									
N	[X/H]	σ	N	[X/H]	σ	N	[X/H]	σ							
FeI	80	-1.633	0.023	101	-1.973	0.021	103	-1.291	0.021
FeII	6	-1.622	0.040	15	-1.980	0.025	18	-1.246	0.022
NaI	1	-2.106	0.081	-0.473	0.081	2	-2.332	0.071	-0.358	0.070	4	-1.429	0.063	-0.138	0.062
MgI	4	-1.565	0.043	0.069	0.040	6	-1.812	0.034	0.161	0.032	5	-1.074	0.040	0.217	0.037
SiI	2	-1.289	0.050	0.345	0.054	0	8	-1.052	0.042	0.240	0.044
CaI	16	-1.479	0.035	0.154	0.032	22	-1.651	0.025	0.322	0.023	16	-1.048	0.031	0.243	0.028
TiI	13	-1.585	0.052	0.048	0.044	9	-1.544	0.042	0.429	0.034	16	-1.157	0.042	0.134	0.036
TiII	4	-1.552	0.045	0.070	0.052	14	-1.723	0.030	0.257	0.030	7	-0.959	0.041	0.287	0.037
CrI	4	-1.651	0.055	-0.018	0.048	4	-1.944	0.048	0.029	0.043	4	-1.283	0.049	0.008	0.043
MnI	3	-2.019	0.063	-0.386	0.059	6	-2.357	0.045	-0.384	0.039	4	-1.688	0.083	-0.397	0.081
NiI	17	-1.730	0.042	-0.097	0.040	8	-2.018	0.059	-0.045	0.058	24	-1.302	0.026	-0.011	0.025
ZnI	2	-1.672	0.043	-0.039	0.048	1	-1.858	0.059	0.116	0.057	2	-1.083	0.036	0.208	0.039
YII	1	-1.900	0.063	-0.278	0.072	1	-2.038	0.079	-0.058	0.079	2	-1.506	0.037	-0.260	0.034
BaII	4	-1.876	0.043	-0.254	0.052	4	-2.332	0.043	-0.352	0.044	4	-1.612	0.043	-0.366	0.040